J. Fluid Mech. (2009), *vol.* 628, *pp.* 121–154. © 2009 Cambridge University Press
doi:10.1017/S0022112009006168 Printed in the United Kingdom

A study of two-dimensional flow past regular polygons via conformal mapping

ZHONG WEI TIAN AND ZI NIU WU†

Department of Engineering Mechanics, Tsinghua University, Beijing 100084, China

(Received 19 June 2008 and in revised form 9 January 2009)

In this paper we study two-dimensional flow around regular polygons with an arbitrary but even number of edges N and one apex pointing to the free stream, with comparison to circular-cylinder flow. Both inviscid flow and low-Reynolds-number viscous flow are addressed. For inviscid flow, we obtained the exact solution for pure potential flow through Schwarz–Christoffel transformation, with the emphasis on the role of edge number, N, on the flow details. We also studied the behaviour, stationary lines and stability of vortex pair and found new stationary lines compared to circular cylinder. For viscous flow we derived the equation of stream function in the mapped (circle) domain, based on which approximate expressions for the critical Reynolds numbers and Strouhal number, as functions of the edge number, are obtained. The Reynolds number is based on the diameter of the circumscribed circle. For the steady flow, the first critical Reynolds number is a monotonically decreasing function of N, while $N \to \infty$ corresponds to that for circular cylinder. The bifurcation point is ahead of the bifurcation point for circular cylinder. For unsteady flow, the critical Reynolds number for vortex shedding and the Strouhal number are both monotonically decreasing functions of N.

1. Introduction

The flow past cylinders contains complex phenomena such as separation and vortex shedding. The basic features of the flow past circular cylinders are well known (see Coutanceau & Daefaye 1991; Williamson 1996). Though a huge amount of results exist for flow around circular cylinder, that around polygons is much less studied. Most of the studies for polygons are for triangles, squares and rectangles, and it is rare to consider polygons with a large N (edge number), with the exceptions of Skews (1991, 1998), who studied autorotational behaviour for polygons with N up to 8, and Tian (1996), who discovered a minimum drag for polygons with $N = 24$ for a range of Reynolds number.

The critical Reynolds numbers for polygons with small number of edges were studied by Okajima (1982), Jackson (1987), Franke (1991) and Klekar & Patankar (1992), amongst others. The first critical Reynolds number, at which separation appears, for the flow past squares with one edge facing the free stream is $Re_{cr1} < 1$ (see Franke 1991), smaller than that for circular cylinder, which is between 5 and 7, varying with researchers (see Taneda 1956; Dennis & Chang 1970; Noack & Eckelmann 1994*b*; Brøns, Jakobsen & Niss 2007). The Reynolds number for squares is based on the side length D_s, while for circular cylinder it is based on the diameter

† Email address for correspondence: ziniuwu@tsinghua.edu.cn

https://doi.org/10.1017/S0022112009006168 Published online by Cambridge University Press

D. The second critical Reynolds number (Re_{cr2}), at which unsteady flow forms, has been studied for the flow past squares with one edge facing the free stream. Okajima (1982) found $Re_{cr2} \leqslant 70$ by experiment, while Klekar & Patankar (1992) got $Re_{cr2} = 50$ by a stability analysis. For triangular cylinder, Jackson (1987) reported the critical Reynolds number to be equal to 34.318 for an isosceles triangle with base 1, height 0.8 and one apex pointing to the free stream, using a finite-element method. The characteristic length in obtaining Re is the base of the isosceles triangle. Zielinska & Wesfreid (1995) numerically investigated the wake of flow past an equilateral triangle and found a critical Reynolds number to be 38.3. This was confirmed experimentally by Wesfreid, Goujon-Durand & Zielinska (1996). As a contrast, the second critical Reynolds number for circular cylinder is about 45–54 (see Jackson 1987; Zebib 1987; Dušek, Gal & Fraunié 1994; Noack & Eckelmann 1994*a*).

Flow structure including the recirculation length and vortex shedding has been studied by Breuer *et al.* (2000) and Sharma & Eswaran (2004), amongst others. For instance, Breuer *et al.* (2000) used the lattice Boltzmann and finite-volume methods to study the non-dimensional recirculation length l_r, defined by the distance from the rear stagnation point to the point at which separated flow reattaches, for channel flow past square cylinder with the block ratio 1/8 and found the fit formula $l_r = -0.065 + 0.0554Re_s$ for $5 \leqslant Re_s \leqslant 60$, where Re_s is the Reynolds number based on the side length, D_s. Sharma & Eswaran (2004) numerically studied the channel flow past square cylinder, with Prandtl number 0.7 and block ratio 5 %, and found $l_r = 0.0685Re_s$ for $5 \leqslant Re_s \leqslant 40$. De & Dalal (2006) numerically studied the open flow past an equilateral triangular cylinder with one apex pointing to the free stream and found the fitted relation $l_r = 0.075Re_s$, for $10 \leqslant Re_s \leqslant 40$. In contrast, for circular cylinder, the fitted relation is $l_r = 0.06710(\pm 0.0008)Re - 0.405(\pm 0.035)$ (see Zielinska *et al.* 1997) or $l_r = 0.068Re - 0.428$ (see Brøns *et al.* 2007). For the unsteady flow past polygons, the Strouhal number increases linearly with $Re^{-1/2}$. For channel flow past square cylinders and triangular cylinders with base 1 and height 0.5, the correlations are $St = 0.2131 - 0.5073/\sqrt{Re_s}$ and $St = 0.2294 - 0.4736/\sqrt{Re_s}$ for $30 \leqslant Re \leqslant 200$, according to the numerical results of Abbassi, Turki & Nasrallah (2002), compared with $St = 0.2684 - 1.0356/\sqrt{Re}$ for the circular situation, experimentally investigated by Fey, König & Eckelmann (1998).

Drag reduction for polygons has been studied by Igarashi & Ito (1993), Igarashi (1997), Sakamoto *et al.* (1997) and Zhou, Cheng & Hung (2005). They used a small rod or a flat plate in the upstream of the cylinder to reduce the drag of square cylinder. Tian (1996) compared the drag coefficient of circular cylinders with those of polygonal cylinders with 15, 18, 24, 30 and 36 sides and found the drag coefficient of polygons with 24 sides decreased 40 % compared with circular cylinder, for $1.2 \times 10^5 < Re < 3.6 \times 10^5$.

Skews (1991, 1998) studied the condition of autorotation for polygons in an upstream vane. He found that only polygons with $N < 8$ can autorotate, and the lift forces generated by rotating polygons are larger than those by spinning circular cylinder at the same rotation speed.

The inviscid flow past polygonal obstacles has been studied using computer for pure potential flow (see Elcrat & Trefethen 1986) and for vortex flows (see Clements 1973; Kiya, Saskai & Arie 1982). For pure potential flow, Elcrat & Trefethen (1986) solved the Kirchhoff flow past polygonal obstacles, including plate with or without spoiler, wedge, equilateral triangle and bracelet, using a Fortran package KIRCH1. For vortex flow, Clements (1973) developed the inviscid model for vortex shedding behind a square-based section and predicted the Strouhal number in good agreement with experimental results. Kiya *et al.* (1982) used the discrete-vortex simulation of the

https://doi.org/10.1017/S0022112009006168 Published online by Cambridge University Press

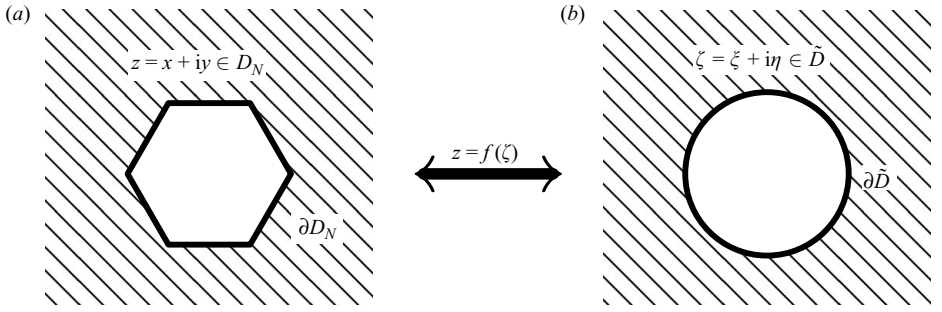


FIGURE 1. Two domains of flow past polygons and their mapping relationship: (*a*) physical domain; (*b*) mapped domain.

separation bubble over a two-dimensional blunt flat plate with finite thickness and right-angled corners and obtained reasonable prediction of time mean and root mean square (r.m.s.) values of the flow field.

In the previous studies for flows around polygons, the number of edges is small. There is no consideration of the influence of the edge number on the general characteristics of the flow. There is no general comparison between the flow around polygons and that around circular cylinders.

In this paper we will address two-dimensional flow past polygons with arbitrary but even number of edges, with one apex pointing to the free stream. The influence of the edge number on the flow characteristics will be specially considered, with comparison to circular cylinders; the latter will be shown to be a special case of polygons when the edge number, N, tends to infinity. In this paper we do not consider odd values of N or the case of inclined flow direction. Some general features of polygon flows compared to those of circular cylinder will be studied by transforming the equations into the mapped domain through Schwarz–Christoffel mapping (see figure 1). The context of this paper is given below.

In § 2, we consider inviscid flow past polygons and analyse the role of the edge number and the difference of flow between polygons and circular cylinders. First we build potential flow solution using Schwarz–Christoffel transformation and compare this solution to circular cylinder. We then consider the stationary lines of vortex pair and study the stability of the vortex pair along its stationary position.

In § 3, we study viscous flow for a Reynolds number low enough to exclude three-dimensional and turbulent effects. By transforming the equation of the stream function to a mapped or circular domain, we analyse the general difference of the flow features, such as the critical Reynolds numbers and Strouhal numbers, between polygons and circular cylinder. Both steady and unsteady flows are addressed. The analysis will be compared to or complemented by computational fluid dynamics (CFD).

The main conclusion will be summarized in § 4.

2. Inviscid flow past polygons

This section is divided into two subsections, respectively devoted to pure potential flow (§ 2.1) and flow with vortex pairs (§ 2.2).

2.1. *Pure potential flow past polygons*

Below we will find the explicit solution, notably pressure coefficient C_p, of the potential flow around polygons through Schwarz–Christoffel mapping. When the solution is

https://doi.org/10.1017/S0022112009006168 Published online by Cambridge University Press

found, we will study the role of the edge number on the pressure distribution on the polygon surface. We will also be interested in whether the case of circular cylinder is a limit of polygonal flow when $N \to \infty$.

It is well known that any polygon can be mapped to a circle (see figure 1) through Schwarz–Christoffel transformation. For regular polygons this transformation is found to be

$$z = f(\zeta) = B\left(\zeta + \frac{\mathrm{e}_1}{\zeta^{N-1}} + \frac{\mathrm{e}_2}{\zeta^{2N-1}} + \frac{\mathrm{e}_3}{\zeta^{3N-1}} + \cdots\right) \tag{2.1}$$

(see Appendix A for derivation). Here B is calculated by (A 5) and e_k by (A 4).

In the mapped domain $\tilde{\mathscr{D}}$, the complex potential $w_B(\zeta)$ is the same as for a circle, i.e.

$$w_B(\zeta) = q\left(\zeta + \frac{1}{\zeta}\right), \quad (\zeta \in \tilde{\mathscr{D}}), \tag{2.2}$$

where $q = U_\infty |f'(\infty)|$ is the free-stream velocity in mapped domain and U_∞ is the free-stream velocity in the physical domain $\mathscr{D}$.

The pressure coefficient $C_{p,N}$ is related to $w_B(\zeta)$ by Bernoulli relation, giving $C_{p,N} = 1 - (1/q^2)|(f'(\infty)/f'(\zeta))(\mathrm{d}w_B/\mathrm{d}\zeta)|^2$. Inserting (2.1) and (2.2) into this we obtain

$$C_{p,N} = 1 - \left|\left(1 - \frac{1}{\zeta^2}\right)\left(1 - \frac{1}{\zeta^N}\right)^{-2/N}\right|^2. \tag{2.3}$$

For $N \to \infty$ we recover the pressure coefficient for circular cylinder

$$C_{p,\infty} = 1 - \left|\left(1 - \frac{1}{\zeta^2}\right)\right|^2, \tag{2.4}$$

since $(1 - 1/\zeta^N)^{-2/N} \to 1$ for $N \to \infty$. This means that in inviscid case flow around a circular cylinder is a limit of flow of polygons when the edge number tends to infinity.

We know that potential flow around a circular cylinder is smooth, but this is, as will be shown, not the case for polygons. Now we study the singularity of the flow and the dependence of the pressure coefficient on the edge number, N. Notably, we will show how fast the solution converges to that of circular cylinder when N increases.

The difference of flow between polygons and circular cylinder can be seen more clearly through $(1 - C_{p,N})/(1 - C_{p,\infty})$, which, when using (2.3) and (2.4), can be expressed as

$$\frac{1 - C_{p,N}}{1 - C_{p,\infty}} = \left|\left(1 - \frac{1}{\zeta^N}\right)^{-4/N}\right| = 1 + O(\rho^{-N}). \tag{2.5}$$

Hence the difference vanishes with the $-N$ power of the distance to the centre $\rho = |\zeta|$, and this difference is evident only near the wall. For region sufficiently far away from the centre, the potential flow for polygons and circular cylinder is the same.

Substituting $\zeta = \mathrm{e}^{\mathrm{i}\phi}$ into (2.3) and (2.4) we find the surface pressure coefficient

$$C_{p,N}^{(s)} = 1 - 4\sin^2\phi \left|2\sin\frac{N\phi}{2}\right|^{-4/N}, \tag{2.6}$$

which reduces to $C_{p,\infty}^{(s)} = 1 - 4\sin^2\phi$ for circular cylinder. For polygons we observe singularity at the apices with an argument $2k\pi/N$, $(k = 1, 2, \ldots, N/2 - 1)$, where $C_{p,N}^{(s)}$ tends to $-\infty$. Figure 2 displays the surface pressure coefficient for some N-sided polygons, comparing with those for the circle. Clearly, a pressure drop exists near

https://doi.org/10.1017/S0022112009006168 Published online by Cambridge University Press

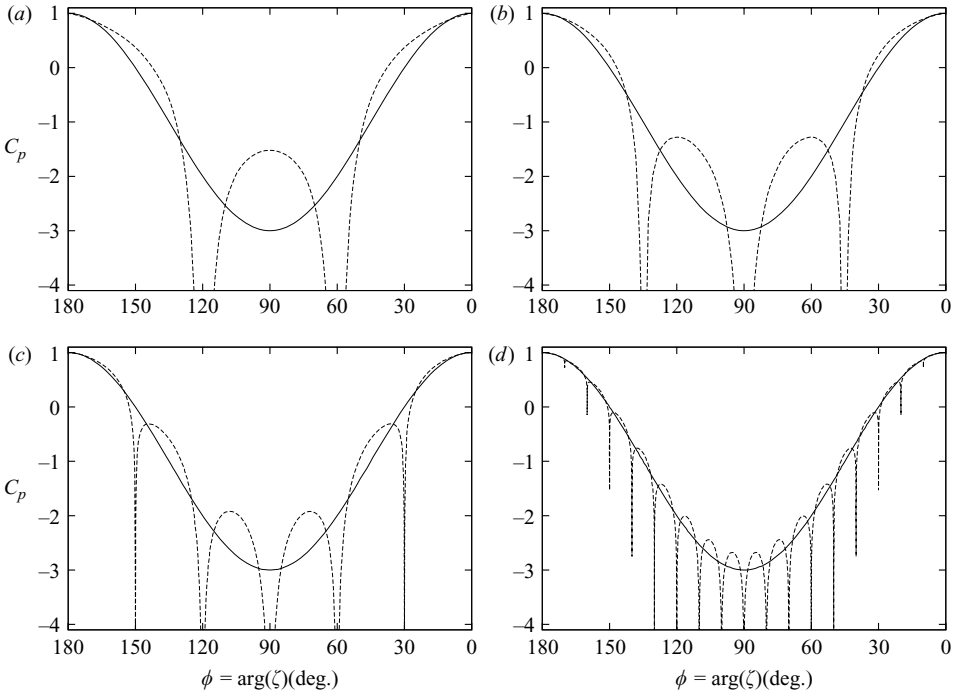


FIGURE 2. Surface pressure coefficient distribution for unit circles and inscribed regular polygons, where solid lines stand for circles and dashed lines for polygons: (*a*) hexagon; (*b*) octagon; (*c*) decagon; (*d*) 36-sided polygon.

each apex, and the magnitude of this drop reflects the intensity of singularity for polygon flow. Clearly, this intensity weakens with increase in N; for instance the range below a certain value, $C_p \leqslant -3$, becomes narrower with the increasing N.

In order to have some global idea for the singularity intensity as a function of the edge number, N, we calculate $\rho_k(C_p = -3)$, the radius of the low-pressure region, namely the region in which the pressure coefficient is below -3. Around each apex z_k we find the contour of $C_p = -3$. Assume this contour intersects the surface at z_k^+ and z_k^- (see figure 3*a*); then the radius $\rho_k(C_p = -3)$ is here defined as

$$\rho_k(C_p = -3) = \sqrt{|(z_k^+ - z_k)(z_k^- - z_k)|}. \tag{2.7}$$

In order to find $z_k^{\pm} = f(\exp(\mathrm{i}\phi_{\pm}))$ we set $C_{p,N}^{(s)}$ defined by (2.6) to -3 so that

$$\left|2\sin\frac{N\phi}{2}\right|^{2/N} - \sin\phi = 0. \tag{2.8}$$

Figure 3(*b*) shows the radius at various apices (numbered as $k = 1, 2, \ldots$, counting from the rear stagnation point) and for various N. Consider for instance $k = 2$, the apex closest to the rear stagnation point; we found a fitted formula $\ln \rho_2 \approx -0.8546N + 2.7298$ according to the data in figure 3(*b*). For other apices, a similar linear relation exists. This means that the radius of low-pressure region around each apex vanishes exponentially with N, i.e. $\rho \sim \mathrm{e}^{-N}$.

https://doi.org/10.1017/S0022112009006168 Published online by Cambridge University Press

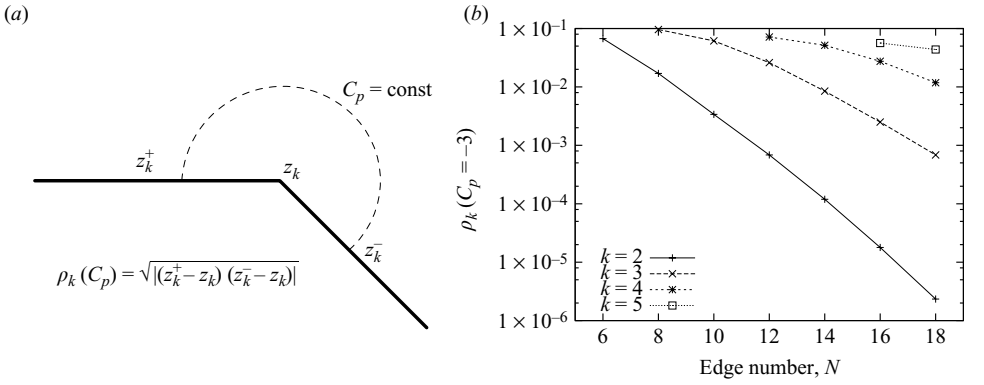


FIGURE 3. Low-pressure region radius of apices on polygon surfaces: (*a*) definition; (*b*) values.

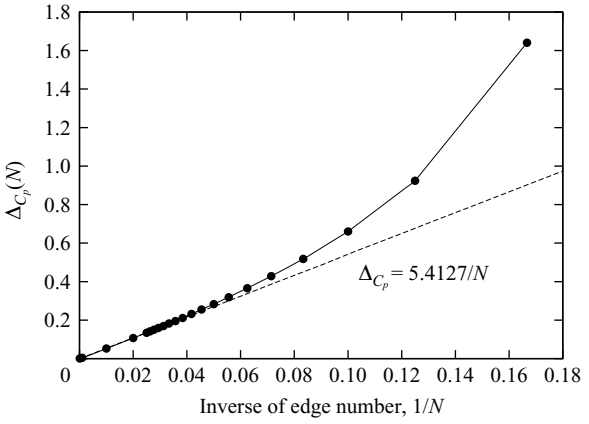


FIGURE 4. Average surface pressure deviation varying with N.

Finally we calculate the overall difference of the surface pressure between polygons and circular cylinder, as defined by

$$\Delta_{C_p}(N) = \frac{1}{\pi}\int_0^{\pi} \left|C_{p,N}^{(s)}(\phi) - C_{p,\infty}^{(s)}(\phi)\right| \mathrm{d}\phi. \tag{2.9}$$

Figure 4 shows the $\Delta_{C_p}(N)$ varying with N. For N sufficiently large, we found that

$$\Delta_{C_p} \approx \frac{5.4127}{N}. \tag{2.10}$$

This means that the global difference of pressure between polygons and circles reduces inversely with N, though the number of singularities is equal to $N-2$.

2.2. *Vortex motion in inviscid flow*

In this subsection we consider the behaviour of vortex pairs around polygons. Vortex pairs around circular cylinder have been studied by Föppl (1913), Elcrat *et al.* (2000), Cai, Liu & Luo (2003) and Zannetti (2006), amongst others. The inviscid separated flows can be regarded as stackings of pure potential and series of point vortices. We are notably interested in the difference of the behaviour of vortex pair between polygons and circular cylinder. In the following we first consider the velocity of vortex

https://doi.org/10.1017/S0022112009006168 Published online by Cambridge University Press

pair compared to circular cylinder. We then study the stationary position of vortex pair. In the end we consider the stability of the stationary position.

2.2.1. *Relationship of vortex velocities between polygons and circles in mapped domain*

The relationship between the velocities of vortices in two domains under a conformal mapping is known as the 'Routh chain rule' (see Routh 1881; Lin 1941; Saffman 1992; Newton 2000). Routh chain rule has already been used to simulate vortex motions outside of many complex shapes, such as square-based section, inclined plane and blunt flat plate with finite thickness (see Clements 1973; Sarpkaya 1975; Kiya *et al.* 1982).

Consider an assembly of M vortices moving inside the physical domain $(x, y) \in \mathscr{D}_N$ (see figure 1*a*). The circulation and position of each vortex respectively are κ_j and $z_j = x_j + \mathrm{i}y_j$, where $j = 1, 2, \ldots, M$. Another circular-boundary physical domain $\mathscr{D}_\infty$ with the same assembly of vortices is considered, which represents the inviscid flow past circles. According to Routh chain rule, the velocities in these two physical domains have a relation as (see Lin 1941*a*, *b*)

$$\dot{z}_j^* = u_{j,N} - \mathrm{i}v_{j,N} = (u_{j,\infty} - \mathrm{i}v_{j,\infty})\frac{1}{f_j'} - \frac{\kappa_j}{4\pi\mathrm{i}}\frac{f_j''}{f_j'^2}, \tag{2.11}$$

where $(u_{j,N}, v_{j,N})$ denotes the velocity of jth vortex outside polygons and $(u_{j,\infty}, v_{j,\infty})$ denotes that outside circles. They are both velocities in physical domain. Equation (2.11) will be used in § 2.2.3 for stability analysis.

Now we derive the vortex velocities in mapped domain in order to have clear comparison with circular cylinder. In mapped domain, the jth vortex has a circulation of κ_j, the same as that in physical domain, as well as a position of $\zeta_j = \xi_j + \mathrm{i}\eta_j$. The position ζ_j is related to z_j by the inverse of Schwarz–Christoffel mapping, i.e. $\zeta_j = f^{-1}(z_j)$. Taking a differential with respect to time gives

$$\dot{\zeta}_j^* = \frac{1}{f_j'^*}\dot{z}_j^* \qquad (j = 1, 2, \ldots, M). \tag{2.12}$$

Substituting (2.11) into (2.12), we obtain the velocity $\dot{\zeta}_j^* = \tilde{u}_j - \mathrm{i}\tilde{v}_j$ of the jth vortex in mapped domain,

$$\tilde{u}_j - \mathrm{i}\tilde{v}_j = (u_{j,\infty} - \mathrm{i}v_{j,\infty})\frac{1}{|f_j'|^2} - \frac{\kappa_j}{4\pi i}\frac{1}{|f_j'|^2}\frac{f_j''}{f_j'}, \tag{2.13}$$

where $(\tilde{u}_j, \tilde{v}_j)$ is defined as the velocity of the jth vortex in mapped domain and $1/|f'|^2$ is the deformation factor γ^2, which will frequently appear in the next parts of this paper and is discussed in Appendix B. Inserting $\gamma^2 = 1/|f'|^2$ into (2.13), we obtain

$$\frac{1}{\gamma^2}(\tilde{u}_j - \mathrm{i}\tilde{v}_j) = (u_{j,\infty} - \mathrm{i}v_{j,\infty}) - \frac{\kappa_j}{4\pi\mathrm{i}}\frac{f_j''}{f_j'}. \tag{2.14}$$

Substituting (B 10) for f''/f' into (2.14) and separating the real and imaginary parts, we obtain

$$\frac{1}{\gamma^2}\tilde{u}_j = u_{j,\infty} - \frac{\kappa_j}{8\pi}\left[\frac{(\gamma^2)_\eta}{\gamma^2}\right]_j, \quad \frac{1}{\gamma^2}\tilde{v}_j = v_{j,\infty} + \frac{\kappa_j}{8\pi}\left[\frac{(\gamma^2)_\xi}{\gamma^2}\right]_j. \tag{2.15}$$

The equations in (2.15) define the relationship of vortex velocities outside of polygons and circles, in the same space (mapped domain). The differences can be

https://doi.org/10.1017/S0022112009006168 Published online by Cambridge University Press

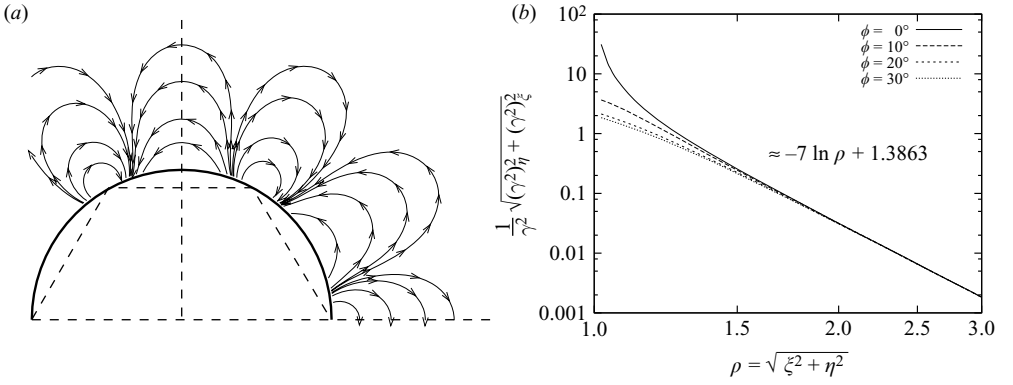


FIGURE 5. Distribution of additional velocities, described by gradients of γ^2: (*a*) directions; (*b*) magnitudes.

divided into two parts: (i) additional velocities corresponding to the second terms in the right of (2.15) and (ii) γ^2 scale of the velocities. The additional velocities are proportional to the circulation κ_j and $(-(\gamma^2)_\eta/\gamma^2, (\gamma^2)_\xi/\gamma^2)$. Figure 5 shows the distribution of $(-(\gamma^2)_\eta/\gamma^2, (\gamma^2)_\xi/\gamma^2)$ in the mapped domain for polygons, e.g. hexagons. Through the directions of the additional velocities we see that, for a vortex with positive circulation, added to the circular case is a clockwise rotation around each apex, compensated by an anticlockwise rotation along each edge. In other words, added to the circular case is a source in the upstream neighbour of each apex and a sink in its downstream neighbour. The magnitude of $(-(\gamma^2)_\eta/\gamma^2, (\gamma^2)_\xi/\gamma^2)$ vanishes linearly with increasing ρ, the distance to the centre, in a double logarithmic figure, with a slope of -7, corresponding to $-N-1$ for hexagons. This means the additional velocity is only evident near the wall, while it vanishes approximately with the $-N-1$ power as ρ increases.

The scaling factor γ^2 (see Appendix B) reaches a maximal value near the apices and a minimal value near the midpoints of edges. This means the vortex near the apices moves fast, while those near the midpoint of edges move slowly in comparison with circular cylinders.

2.2.2. *Stationary lines of vortex pair for polygons*

In this subsection we study the stationary lines of symmetric vortex pair outside of polygons, by using the stationary condition outside symmetric bluff bodies proposed by Zannetti (2006). Stationary lines are positions at which the vortex pair does not move.

Assume that in the inviscid flow past polygons or circles, a symmetric vortex pair with circulations $\mp\kappa$ locates at ζ and ζ^* in mapped domain. Here ζ^* is the conjugate of ζ and represents the location of the lower vortex.

A convenient stationary condition of a pair of vortex with circulations $\mp\kappa$ and locating at z_0 and z_0^* in physical domain was derived by Zannetti (2006). This condition is expressed as

$$\mathrm{Re}\left[\frac{\mathrm{d}^2 w_B/\mathrm{d}z^2}{(\mathrm{d}w_B/\mathrm{d}z)^2}\right] = 0 \tag{2.16a}$$

https://doi.org/10.1017/S0022112009006168 Published online by Cambridge University Press

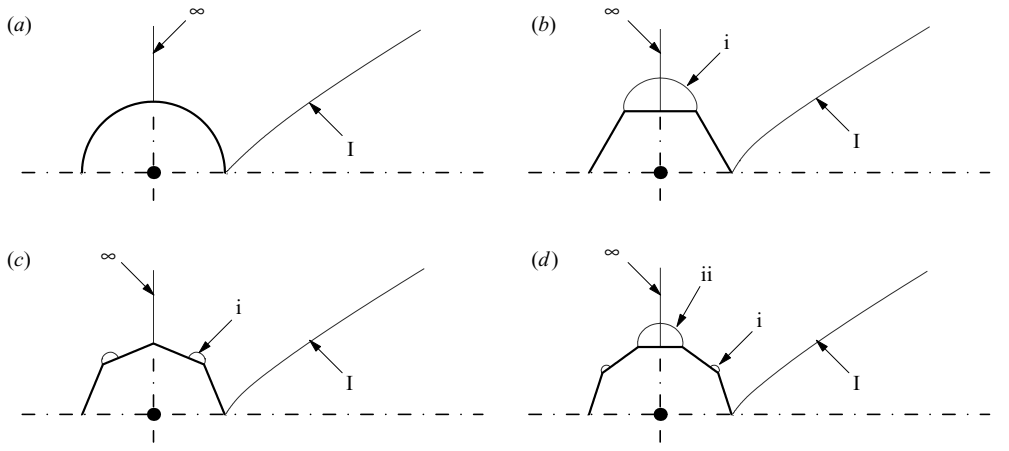


FIGURE 6. Stationary lines for unit circles and their inscribed polygons: (*a*) unit circles; (*b*) hexagons; (*c*) octagons; (*d*) decagons.

for the stationary position and

$$\kappa = 4\pi \left\{ \frac{1}{\mathrm{Im}(w_B)} + \mathrm{Im}\left[\frac{\mathrm{d}^2 w_B/\mathrm{d}z^2}{(\mathrm{d}w_B/\mathrm{d}z)^2} \right] \right\}^{-1} \tag{2.16b}$$

for the corresponding circulation. Here w_B is the pure complex potential.

Substituting (2.1) and (2.2) into (2.16*a*) gives

$$\mathrm{Re}\left[\frac{\mathrm{d}^2 w_B/\mathrm{d}z^2}{(\mathrm{d}w_B/\mathrm{d}z)^2} \right] = \mathrm{Re}\left[\frac{2\zeta}{q(\zeta^2-1)^2} \left(1 - \frac{\zeta^2-1}{\zeta^N-1} \right) \right] = 0. \tag{2.17}$$

Figure 6 shows the stationary lines for a vortex pair obtained from (2.17). For the circular case, there are two stationary lines, the well-known Föppl line I (see Föppl 1913; Elcrat *et al.* 2000; Zannetti 2006) starting from the rear stagnation point and the ∞ line starting from the upper point of the circle. The Föppl line has a trajectory $\rho^2 - 1 = 2\rho\eta$ and a circulation $\kappa = 4\pi q\eta(1 - 1/r^4)$.

For polygons, besides line I and the ∞ line which are similar to the circular case, we observe additional lines: i, ii, ... These lines start from the apices and end at edges or others apices. Namely these additional lines form closed curves with the edges. These closed regions grow smaller with increasing N, see the three curves denoted as i in figure 6(*b–d*) for example. When $N \to \infty$, the additional lines disappear, and we recover the situation of circular cylinder.

2.2.3. *Stability of stationary vortex pair for polygons*

We study the stability of a symmetric stationary vortex pair outside of polygons, using a linear stability analysis method (see Tang & Aubry 1997; Shashikanth *et al.* 2002; Cai *et al.* 2003; Protas 2007).

Assume that a vortex pair with a circulation $\mp\kappa$ locates at $z_0 = x_0 + \mathrm{i}y_0$ and $z_0^* = x_0 - \mathrm{i}y_0$ in physical domain. Suppose the vortex pair undergoes a small arbitrary displacement, changing from z_0 and z_0^* to z_1 and z_2, respectively.

According to Shashikanth *et al.* (2002), Cai *et al.* (2003) and Protas (2007), the displacement can be decomposed as a symmetric mode and an antisymmetric mode:

$$\text{symmetric:}\quad z_1 = z_0 + \Delta z \equiv z, \quad z_2 = z_0^* + \Delta z^* \equiv z^*, \tag{2.18a}$$

$$\text{antisymmetric:}\quad z_1 = z_0 + \Delta z \equiv z, \quad z_2 = z_0^* - \Delta z^* \equiv 2z_0^* - z^*. \tag{2.18b}$$

https://doi.org/10.1017/S0022112009006168 Published online by Cambridge University Press

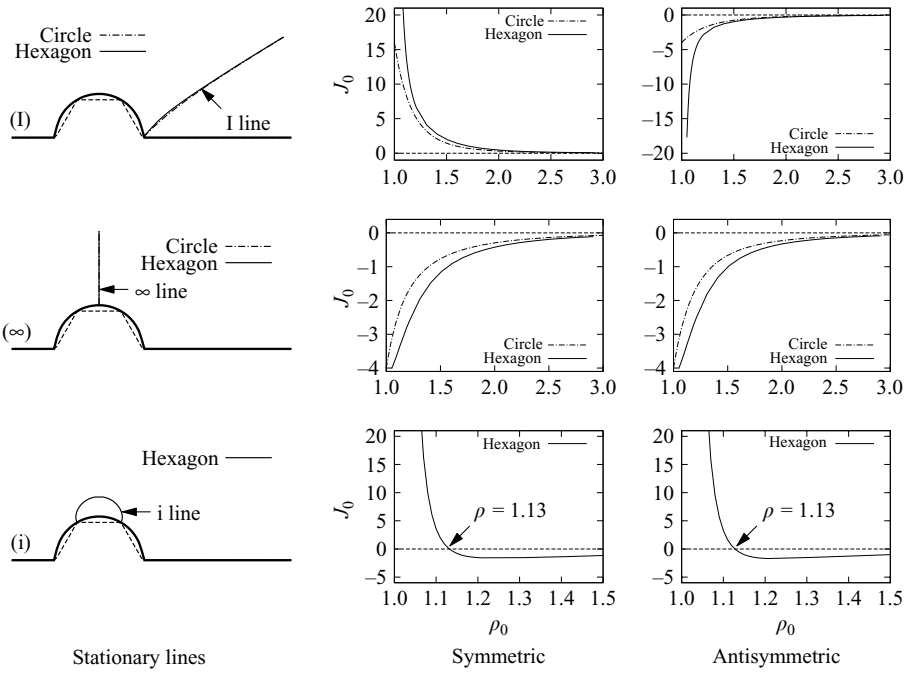


FIGURE 7. Invariants varying with positions for circles and hexagons.

Considering the upper vortex at $z = x + \mathrm{i}y$, the velocity of the vortex centre is (u, v), where the subscript 1 is dropped for simplicity. Expanding (u, v) around (x_0, y_0) to first order gives $\dot{\boldsymbol{X}} = \boldsymbol{D}\boldsymbol{X}$, where $\boldsymbol{X} = (x - x_0, y - y_0)^T$; $\dot{\boldsymbol{X}} = (u, v)^T$; and $\boldsymbol{D} = |\partial(u, v)/\partial(x, y)|_0$ is a 2×2 Jacobian matrix. The invariants of $\boldsymbol{D}$ are computed as

$$D_0 \equiv \mathrm{tr}(\boldsymbol{D}) = \lambda_1 + \lambda_2, \quad J_0 \equiv |\boldsymbol{D}| = \lambda_1 \cdot \lambda_2, \tag{2.19}$$

where λ_1 and λ_2 are the eigenvalues of $\boldsymbol{D}$.

Cai *et al.* (2003) proved that the first invariant D_0 is zero under both symmetric and antisymmetric disturbances, and the stability can be determined by the second invariant J_0: $J_0 > 0$ corresponds to a neutral stable centre, while $J_0 < 0$ corresponds to an unstable saddle.

Now we follow Cai *et al.* (2003) to compute the second invariant, J_0. First we need to know the vortex velocities. For circle, the vortex velocity at z is given by (see Cai *et al.* 2003)

$$u_\infty - \mathrm{i}v_\infty = q\left(1 - \frac{1}{z_1^2}\right) - \frac{\kappa}{2\pi i}\left(\frac{1}{z_1 - 1/z_2^*} - \frac{1}{z_1 - z_2} - \frac{1}{z_1 - 1/z_1^*}\right), \tag{2.20}$$

where z_1 and z_2 are calculated by (2.18) for both symmetric and antisymmetric modes. Substituting (2.20) into (2.11) gives the velocities of the vortex pair outside of polygons. We calculate the Jacobian matrix, $\boldsymbol{D}$, using a standard fourth-order accurate finite-difference algorithm. Once $\boldsymbol{D}$ is obtained, we compute J_0 by $J_0 = |\boldsymbol{D}|$.

Figure 7 shows J_0 for hexagon, compared to J_0 for circular cylinder. For the circular case, on the Föppl line I, the vortex pair is neutral stable ($J_0 > 0$) under symmetric perturbations and unstable ($J_0 < 0$) under antisymmetric perturbations, as already shown by Cai *et al.* (2003). On the ∞ line, the vortex pair is always unstable ($J_0 < 0$) under both symmetric and antisymmetric perturbations.

https://doi.org/10.1017/S0022112009006168 Published online by Cambridge University Press

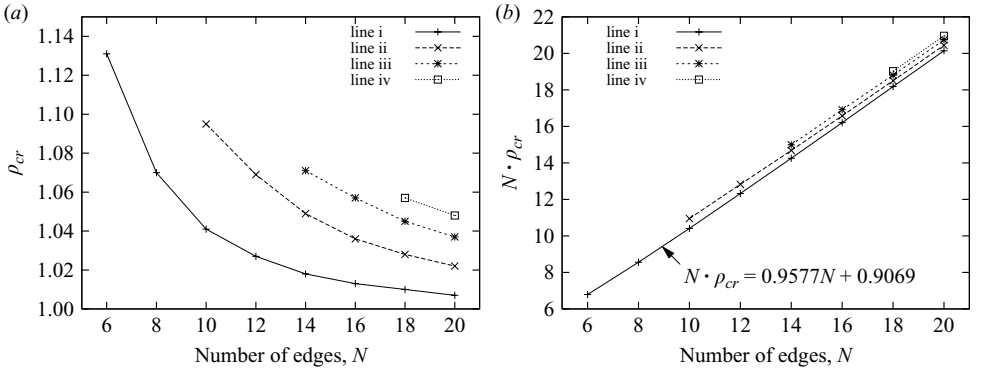


FIGURE 8. Critical radius for stabilities at different closed stationary lines: (*a*) ρ_{cr} versus N; (*b*) $N \cdot \rho_{cr}$ versus N.

For hexagons, the stabilities for vortex pair at line I and the ∞ line are the same as those of circular cylinder. On the closed line i, we observe that the stabilities depend on ρ, the distance of the vortex to the origin, independent of perturbation modes. The vortex pair is neutral stable when $\rho < 1.131$ while unstable when $\rho > 1.131$.

For the other polygons, we also find that the stabilities for vortex pair at the close lines i, ii, ..., are independent of perturbation modes. On these closed lines, the vortex pair is neutral stable when ρ is less than a critical radius, ρ_{cr}, and unstable when $\rho > \rho_{cr}$. This critical radius is shown in figure 8 for different closed stationary lines outside of N-sided polygons. We find that a linear relationship between $N \cdot \rho_{cr}$ and N for a certain closed stationary lines. For the critical radius for line i outside of N-sided polygons, we find $N \cdot \rho_{cr} = 0.9577N + 0.9069$ and $\rho_{cr} = 0.9577 + 0.9069/N$.

3. Two-dimensional viscous flow past polygons

In this section we derive the equation of stream function ψ in the mapped (circle) domain. Though it is not conformally invariant, it can be used to find the critical Reynolds number and Strouhal numbers varying with N for steady and unsteady flows, respectively (see § 3.2 and § 3.3).

3.1. *Equation of stream function in mapped domain*

The equation of stream function ψ for flow past polygons in physical domain can be expressed as

$$\omega_t - \mathscr{J}(\psi, \omega) - \frac{2}{Re}\nabla^2\omega = 0, \qquad (x, y) \in \mathscr{D}_N, \tag{3.1a}$$

$$\psi = 0, \quad \nabla\psi = 0, \qquad (x, y) \in \partial\mathscr{D}_N, \tag{3.1b}$$

$$\psi_x = 0, \quad \psi_y = 1, \qquad \sqrt{x^2 + y^2} \to \infty. \tag{3.1c}$$

Here $\omega = -\nabla^2\psi$ stands for the vorticity, and $\mathscr{J}(\psi, \omega) = (\psi)_x(\omega)_y - (\psi)_y(\omega)_x$ corresponds to the convection term. The Reynolds number, Re, is defined as $Re = (l_{ref} v_\infty)/\nu$, where v_∞ is the incoming free-stream velocity; ν is the kinematical viscosity; and l_{ref} is the reference length for polygons. Throughout this paper we use $l_{ref} = 2R_{max}$, where R_{max} is the radius of the circumscribed circle for polygon. Later on in § 3.1 we also consider another possible choice.

Now we will transform this equation into the form in mapped domain $(\xi, \eta) \in \tilde{\mathscr{D}}$. The two domains have a relation described by a conformal mapping $z = x$

https://doi.org/10.1017/S0022112009006168 Published online by Cambridge University Press

$+ \mathrm{i}y = f(\zeta) = x(\xi, \eta) + \mathrm{i}y(\xi, \eta)$. The differential relation between (x, y) and (ξ, η) can be derived by Cauchy–Riemann condition (see (B 1)). Thus the Lame coefficient for coordinate (ξ, η) satisfies $h_\xi = h_\eta = |f'|$. Thereupon, using these Lame coefficients, we can transform the operators in (3.1) into the mapped domain,

$$\nabla^2\psi = \gamma^2(\tilde{\nabla}^2\psi), \tag{3.2a}$$

$$\nabla^4\psi = \gamma^2(\tilde{\nabla}^2\gamma^2)(\tilde{\nabla}^2\psi) + 2\gamma^2(\tilde{\nabla}^2\gamma^2)\cdot[\tilde{\nabla}(\tilde{\nabla}^2\psi)] + \gamma^4(\tilde{\nabla}^4\psi), \tag{3.2b}$$

$$\mathscr{J}(\psi, \nabla^2\psi) = \gamma^2(\tilde{\nabla}^2\psi)\tilde{\mathscr{J}}(\psi, \gamma^2) + \gamma^4\tilde{\mathscr{J}}(\psi, \tilde{\nabla}^2\psi), \tag{3.2c}$$

where $\gamma^2 = 1/|f'|^2$, the deformation factor, is given in Appendix B, and the operators in mapped domain are defined as

$$\tilde{\nabla} = (\partial_\xi, \partial_\eta), \tilde{\nabla}^2 = \partial_{\xi\xi} + \partial_{\eta\eta}, \tilde{\mathscr{J}}(*, \circ) = (*)_\xi(\circ)_\eta - (*)_\eta(\circ)_\xi. \tag{3.3}$$

Now we derive the boundary conditions in the mapped domain. First we consider the boundary condition at infinity, $\sqrt{\xi^2 + \eta^2} \to \infty$. Since $\psi_\xi = \psi_x x_\xi + \psi_y y_\xi$ and $\psi_\eta = \psi_x x_\eta + \psi_y y_\eta$, by using (3.1$c$) and the differential relationship (B 1), ψ_ξ and ψ_η at infinity can be simplified as

$$\psi_\xi = \mathrm{Im}[f'(\infty)], \quad \psi_\eta = \mathrm{Re}[f'(\infty)]. \tag{3.4}$$

Since $f'(\infty) = B = 1/\Upsilon$ according to (B 3) and (B 7), (3.4) reduces to

$$\psi_\xi = 0, \quad \psi_\eta = 1/\Upsilon. \tag{3.5}$$

Equation (3.5) is slightly different from (3.1c). In order to have the same form, we define $\tilde{\psi} = \Upsilon\psi$ as the stream function in mapped domain, so that (3.5) reduces to

$$\tilde{\psi}_\xi = 0, \quad \tilde{\psi}_\eta = 1, \qquad \sqrt{\xi^2 + \eta^2} \to \infty, \tag{3.6}$$

which is the boundary condition at infinity in mapped domain. The boundary condition at the wall,

$$\tilde{\psi} = 0, \quad \tilde{\nabla}\tilde{\psi} = 0, \qquad (\xi, \eta) \in \partial\tilde{\mathscr{D}}, \tag{3.7}$$

can be easily derived by using (3.1b).

Next we consider the equation of $\tilde{\psi}$ in mapped domain. Substituting $\tilde{\psi} = \Upsilon\psi$ into (3.2), we obtain

$$\nabla^2\psi = \frac{\gamma^2}{\Upsilon}(\tilde{\nabla}^2\tilde{\psi}), \tag{3.8a}$$

$$\nabla^4\psi = \frac{\gamma^2}{\Upsilon}(\tilde{\nabla}^2\gamma^2)(\tilde{\nabla}^2\tilde{\psi}) + \frac{2\gamma^2}{\Upsilon}(\tilde{\nabla}^2\gamma^2)\cdot[\tilde{\nabla}(\tilde{\nabla}^2\tilde{\psi})] + \frac{\gamma^4}{\Upsilon}(\tilde{\nabla}^4\tilde{\psi}), \tag{3.8b}$$

$$\mathscr{J}(\psi, \nabla^2\psi) = \frac{\gamma^2}{\Upsilon^2}(\tilde{\nabla}^2\tilde{\psi})\tilde{\mathscr{J}}(\tilde{\psi}, \gamma^2) + \frac{\gamma^4}{\Upsilon^2}\tilde{\mathscr{J}}(\tilde{\psi}, \tilde{\nabla}^2\tilde{\psi}). \tag{3.8c}$$

Substituting (3.8) into (3.1), eliminating the operators in physical domain and multiplying the result by Υ^2/γ^4, we obtain

$$\frac{\Upsilon}{\gamma^2}(\tilde{\nabla}^2\tilde{\psi})_t - \tilde{\mathscr{J}}(\tilde{\psi}, \tilde{\nabla}^2\tilde{\psi}) - \frac{2}{Re_{eq}}(\tilde{\nabla}^4\tilde{\psi}) = \frac{2}{Re_{eq}}\frac{\tilde{\nabla}^2\gamma^2}{\gamma^2}(\tilde{\nabla}^2\tilde{\psi}) + \frac{4}{Re_{eq}}\frac{\tilde{\nabla}\gamma^2}{\gamma^2}\cdot[\tilde{\nabla}(\tilde{\nabla}^2\tilde{\psi})] + \frac{1}{\gamma^2}\tilde{\mathscr{J}}(\tilde{\psi}, \gamma^2)(\tilde{\nabla}^2\tilde{\psi}), \tag{3.9}$$

https://doi.org/10.1017/S0022112009006168 Published online by Cambridge University Press

where

$$Re_{eq} = Re/\Upsilon \tag{3.10}$$

will be called the equivalent Reynolds number. Defining the vorticity in mapped domain as $\tilde{\omega} = -\tilde{\nabla}^2\psi$, substituting it into (3.9) and replacing $\tilde{\nabla}^2\tilde{\psi}$ with $-\tilde{\omega}$, we obtain the vorticity-stream equation in the mapped domain,

$$\frac{\Upsilon}{\gamma^2}\tilde{\omega}_t - \tilde{\mathscr{J}}(\tilde{\psi}, \tilde{\omega}) - \frac{2}{Re_{eq}}\tilde{\nabla}^2\tilde{\omega} = S_1 + S_2 + S_3, \tag{3.11}$$

where

$$S_1 = \frac{2}{Re_{eq}}\frac{\tilde{\nabla}^2\gamma^2}{\gamma^2}\tilde{\omega}, \quad S_2 = \frac{4}{Re_{eq}}\frac{\tilde{\nabla}\gamma^2}{\gamma^2}\cdot(\tilde{\nabla}\tilde{\omega}), \quad S_3 = \frac{1}{\gamma^2}\tilde{\mathscr{J}}(\tilde{\psi}, \gamma^2)\tilde{\omega} \tag{3.12}$$

are three additional source terms. Now we summarize the equation and boundary conditions for the stream function in mapped domain:

$$\frac{\Upsilon}{\gamma^2}\tilde{\omega}_t - \tilde{\mathscr{J}}(\tilde{\psi}, \tilde{\omega}) - \frac{2}{Re_{eq}}\tilde{\nabla}^2\tilde{\omega} = S_1 + S_2 + S_3, \qquad (\xi, \eta) \in \tilde{\mathscr{D}}, \tag{3.13a}$$

$$\tilde{\psi} = 0, \quad \tilde{\nabla}\tilde{\psi} = 0, \qquad (\xi, \eta) \in \partial\tilde{\mathscr{D}}, \tag{3.13b}$$

$$\tilde{\psi}_\xi = 0, \quad \tilde{\psi}_\eta = 1, \qquad \sqrt{\xi^2 + \eta^2} \to \infty. \tag{3.13c}$$

For the circular situation, the equations in mapped and physical domains are the same, which are

$$\omega_t - \mathscr{J}(\psi, \omega) - \frac{2}{Re}\nabla^2\omega = 0, \qquad (x, y) \in \mathscr{D}_\infty, \tag{3.14a}$$

$$\psi = 0, \quad \nabla\psi = 0, \qquad (x, y) \in \partial\mathscr{D}_\infty, \tag{3.14b}$$

$$\psi_x = 0, \quad \psi_y = 1, \qquad \sqrt{x^2 + y^2} \to \infty. \tag{3.14c}$$

The reference length in (3.14) is $l_{ref} = 2R$, where R is the radius of the circle.

The differences between (3.13) and (3.14) are divided into three parts:

(*a*) the Reynolds number in (3.14) is changed into an equivalent value $Re_{eq} = Re/\Upsilon$ in (3.13);

(*b*) a scaling factor γ^2/Υ appears before time derivative in (3.13);

(*c*) three additional source terms are added to the right-hand side of (3.13).

We have shown in Appendix B that Υ for each N-sided polygon is larger than 1 (see (B 7) and figure 21). Accordingly, the equivalent Reynolds number, Re_{eq}, is smaller than Re.

If we choose an N-dependent length scale for Re, then we will have a different scaling factor. For instance, we may use $l_{ref} = 2R_{mean}$ with

$$R_{mean} = \exp[(1/2\pi)\int_{-\pi}^{\pi} \log R(\varphi)\,\mathrm{d}\varphi]. \tag{3.15}$$

It can be proven that

$$R_{mean} = R_{max}/\Upsilon. \tag{3.16}$$

In this way the equivalent or critical Reynolds number is the same as that for a circle. The choice of different length scale does not affect the conclusions drawn in this paper, though in general the critical values depend on the length scale and may suggest different properties of the flow pattern (see Batchelor 1967).

https://doi.org/10.1017/S0022112009006168 Published online by Cambridge University Press

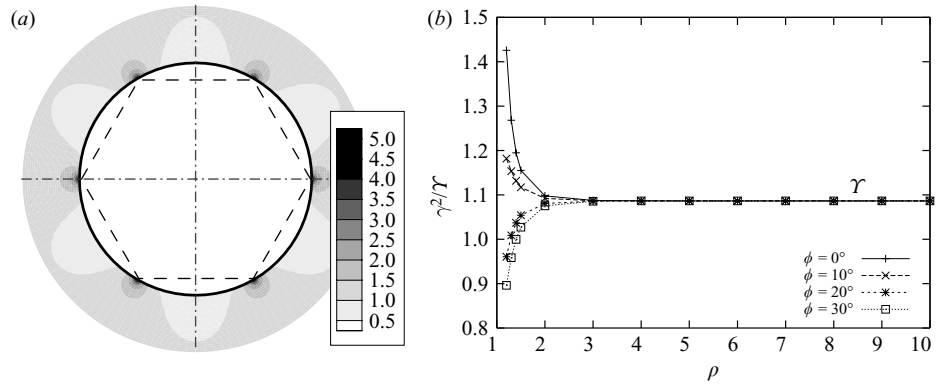


FIGURE 9. (*a*) Contour and (*b*) radial distribution of time-scaling factor, γ^2/Υ, in mapped domain.

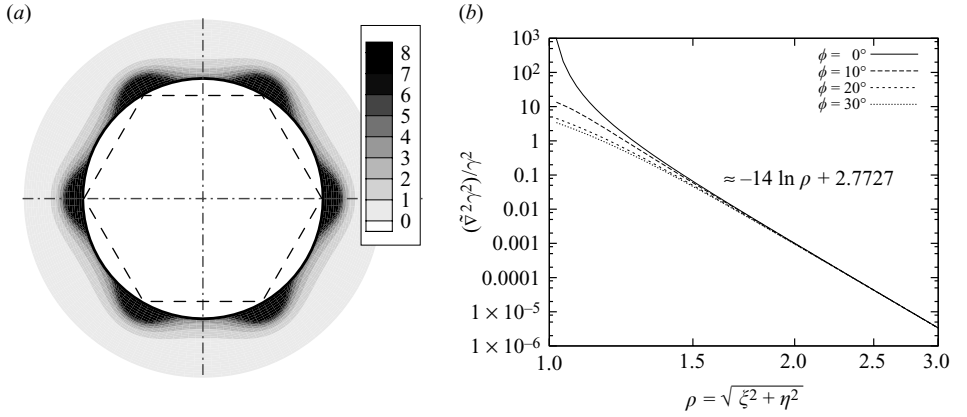


FIGURE 10. Distribution of $\tilde{\nabla}^2\gamma^2/\gamma^2$ in mapped domain for hexagons: (*a*) contour; (*b*) magnitude.

For the time-scaling factor, γ^2/Υ, we can easily obtain the distribution by dividing (B 4) by (B 7). Figure 9 shows the distribution of γ^2/Υ in mapped domain. In most regions not quite near the wall, especially far away from the wall, $\gamma^2/\Upsilon \approx \Upsilon$.

The factor $\tilde{\nabla}^2\gamma^2/\gamma^2$ in source term S_1 can be expressed as

$$\frac{\tilde{\nabla}^2\gamma^2}{\gamma^2} = \frac{16}{\rho^2(\rho^{2N} - 2\rho^N \cos N\phi + 1)} \tag{3.17}$$

(see Appendix B for the derivation). Figure 10 shows the distribution of $\tilde{\nabla}^2\gamma^2/\gamma^2$ in mapped domain: $\tilde{\nabla}^2\gamma^2/\gamma^2$ tends to infinity at the apices, while it vanishes quickly far away from walls. Figure 10(*b*) shows that $\tilde{\nabla}^2\gamma^2/\gamma^2$ vanishes linearly with increasing ρ, the distance to the centre, in a double logarithmic figure, with a slope of -14, corresponding to $-2N-2$ for hexagon. This means the source term S_1 is only evident near the wall, while it vanishes approximately with the $-2N-2$ power as ρ increases.

https://doi.org/10.1017/S0022112009006168 Published online by Cambridge University Press

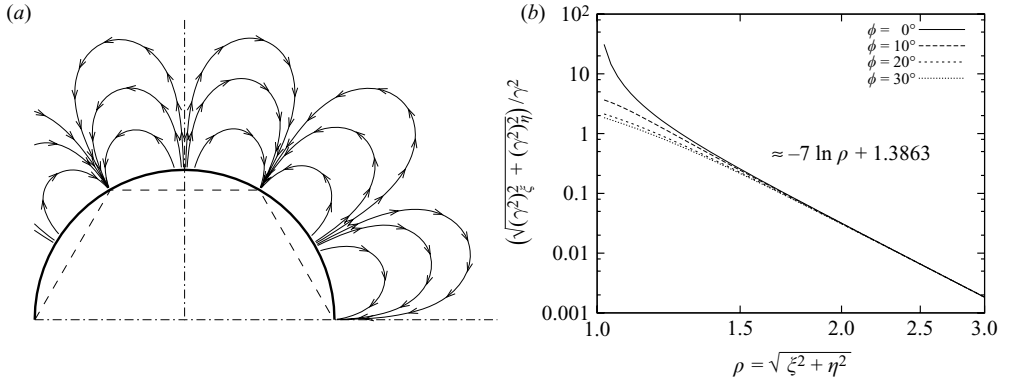


FIGURE 11. Distribution of $(\tilde{\nabla}\gamma^2)/\gamma^2$ in mapped domain for hexagons: (*a*) direction; (*b*) magnitude.

The source term S_2 is expressed as the dot product of two gradient vectors $\tilde{\nabla}\tilde{\omega}$ and $\tilde{\nabla}\gamma^2/\gamma^2$. The distribution of $\tilde{\nabla}\gamma^2/\gamma^2$ in mapped domain can be expressed as

$$\frac{(\gamma^2)_\rho}{\gamma^2} = -\frac{4}{\rho}\left(\frac{\rho^N \cos N\phi - 1}{\rho^{2N} - 2\rho^N \cos N\phi + 1}\right), \tag{3.18a}$$

$$\frac{1}{\rho}\frac{(\gamma^2)_\phi}{\gamma^2} = -\frac{4}{\rho}\left(\frac{\rho^N \sin N\phi}{\rho^{2N} - 2\rho^N \cos N\phi + 1}\right) \tag{3.18b}$$

(see Appendix B for the derivation). Figure 11 shows the direction and magnitude of $(\tilde{\nabla}\gamma^2)/\gamma^2$ in mapped domain. The source term S_2 is only significant near the wall and vanishes approximately with the $-N-1$ power as ρ increases.

The source term S_3 is proportional to $\tilde{\omega}$, with the proportional coefficient $\tilde{\mathscr{J}}(\tilde{\psi}, \gamma^2)$. However, the convection is weak ($\tilde{\psi}_\xi \approx 0, \tilde{\psi}_\eta \approx 0$) in regions near the wall, and the relative gradient γ^2 is weak in regions far from the walls.

Now we consider the possible roles of the equivalent Reynolds number, the time-scaling factor and the three source terms.

Since the Reynolds number is replaced by the equivalent one, the flow around polygons at a Reynolds number Re should be to some extent similar to the flow around circular cylinder at the equivalent Reynolds number $Re_{eq} = Re/\Upsilon$. We will show in § 3.2 and § 3.3 that the critical Reynolds numbers for separation and vortex shedding are indeed related to the equivalent one.

The time-scaling factor should affect the frequency of the unsteadiness of the flow; this will become clear in § 3.3.

The three source terms should have some role on the details of the flow and would have some combined roles together with the equivalent Reynolds number and the time-scaling factor. But their roles, in the critical Reynolds numbers and the frequency of unsteadiness, should be minor as compared to the equivalent Reynolds number and time-scaling factor. Hence, in the following analysis, we will omit the influence of the three source terms. The qualitative conclusion based on the theoretical reasoning will be supported or complemented by CFD. The CFD package solves the problem in physical domain (not the transformed one) and is mainly used to check out or complement the theoretical results.

https://doi.org/10.1017/S0022112009006168 Published online by Cambridge University Press

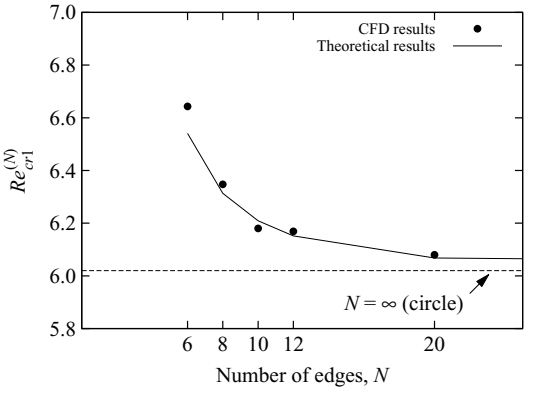


FIGURE 12. First critical Reynolds number, $Re_{cr1}^{(N)}$, for various N-sided polygons.

3.2. *Steady flows past polygons*

In this subsection, we first study the relationship in critical Reynolds numbers between polygons and circles. Next we discuss the difference in flow patterns between polygons and circles, including location of bifurcation points, streamline topologies before or after bifurcations.

3.2.1. *First critical Reynolds number*

We have shown that in the mapped domain, the Reynolds number for polygons is replaced by the equivalent one, $Re_{eq} = Re/\Upsilon$, comparing Re for circles. Hence we conjecture that the critical Reynolds number would be determined by the equivalent ones, i.e. $Re_{eq,cr1} = Re_{cr1}^{(\infty)}$. This means that

$$Re_{cr1}^{(N)} \approx \Upsilon Re_{cr1}^{(\infty)} = \frac{N}{\pi} \sin\left(\frac{N-1}{N}\pi\right) \Gamma\left(\frac{N-1}{N}\right)^2 \Gamma\left(\frac{N+2}{N}\right) Re_{cr1}^{(\infty)}, \tag{3.19}$$

where $Re_{cr1}^{(N)}$ and $Re_{cr1}^{(\infty)}$ are the first critical Reynolds numbers for an N-sided polygon and circular cylinder respectively. According to figure 21 in Appendix A, Υ in (3.19) is larger than unit and is a monotonically decreasing function of N. As $N \to \infty$, $Re_{cr1}^{(N)}$ asymptotically tends to $Re_{cr1}^{(\infty)}$. For example, the difference between $Re_{cr1}^{(N)}$ and $Re_{cr1}^{(\infty)}$ is less than 5 % when $N \geqslant 8$ and is less than 1 % when $N \geqslant 18$. Since $\Upsilon > 1$, (3.19) means that flow around polygons separates at a Reynolds number larger than that around a circular cylinder, and the critical Reynolds number is a monotonically decreasing function of N. In order to see if this is indeed so, we display in figure 12 the critical Reynolds numbers obtained by CFD (Appendix C). We observe that the CFD result follows qualitatively with (3.19).

3.2.2. *Locations of vortex cores and bifurcation points*

Now we use CFD to analyse the location of vortex cores and bifurcation points. For circular cylinder, we know that when Re reaches $Re_{cr1} \approx 6$, a pair of counter-rotating separation bubbles firstly appear at the rear stagnation point. As Re increases, the recirculation regions grow larger, and the separation points move ahead. For polygons, we also find these phenomena, while some details are different.

Figure 13(a) shows the position of vortex cores at different Reynolds numbers for flow past circles and hexagons in mapped domain. We find that the vortex cores outside of hexagons are slightly higher than those outside of circles. Moreover,

https://doi.org/10.1017/S0022112009006168 Published online by Cambridge University Press

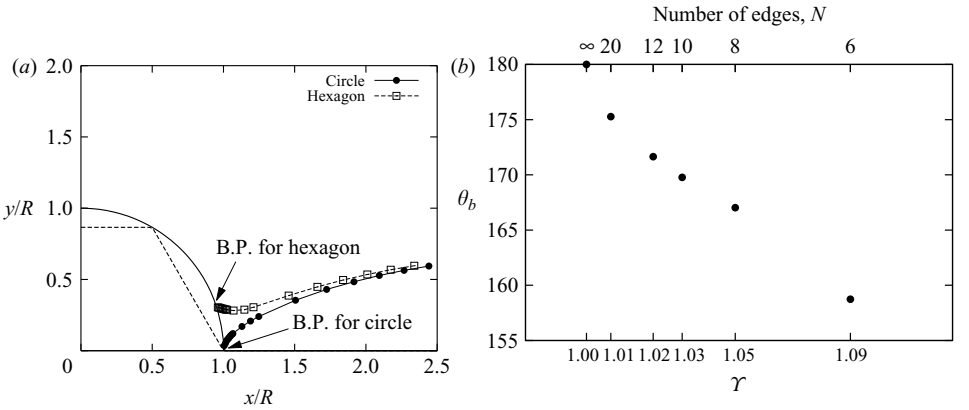


FIGURE 13. Positions of (*a*) vortex cores and (*b*) bifurcation points (B.P.) for flow past polygons and circles, where θ_b is the azimuthal angle of bifurcation point measured from the front stagnation point.

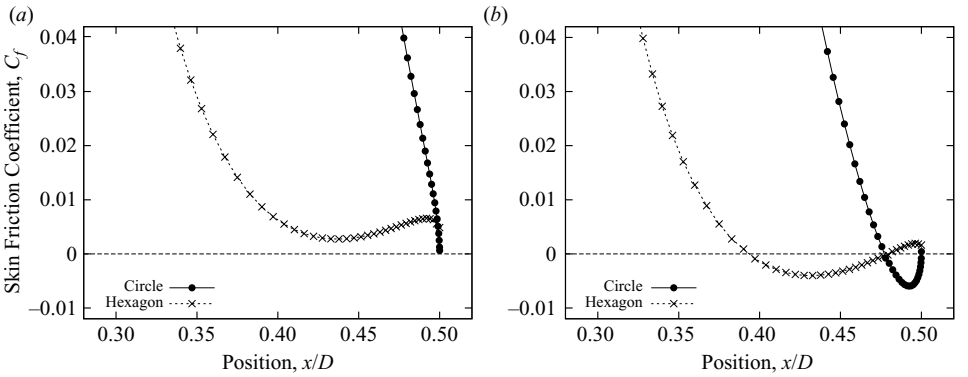


FIGURE 14. Surface shear stress coefficient on the aft half parts of surfaces for hexagons and circles (*a*) before separation and (*b*) after separation.

the vortex cores for hexagons do not approach to the rear stagnation point as *Re* decreases but some point at the last edges, away from the rear stagnation point.

The intersection point of the line of vortex cores at different Reynolds numbers with the wall coincides with the bifurcation point, where separation firstly appears. According to figure 13(*a*), the bifurcation point for hexagons is not the same as that for circles. For the other polygons, we also find that the bifurcation point locates at some point ahead of the rear stagnation point (see figure 13*b*).

The difference of locations of bifurcation points is concerned with the surface shear stress. Figure 14 shows the surface shear stress coefficient on the aft half parts of surfaces for hexagon and circular cylinder according to CFD results. Before bifurcation, corresponding to figure 14(*a*), we find that a local minimum value appears for hexagon at $Re = 6.5$ before the rear stagnation point. This minimum value decreases as *Re* increases, and when a negative value is first reached, the separation starts. After bifurcation, corresponding to figure 14(*b*), there are two zero points of surface shear stress coefficient on hexagon surface, corresponding to separation and reattachment, respectively.

https://doi.org/10.1017/S0022112009006168 Published online by Cambridge University Press

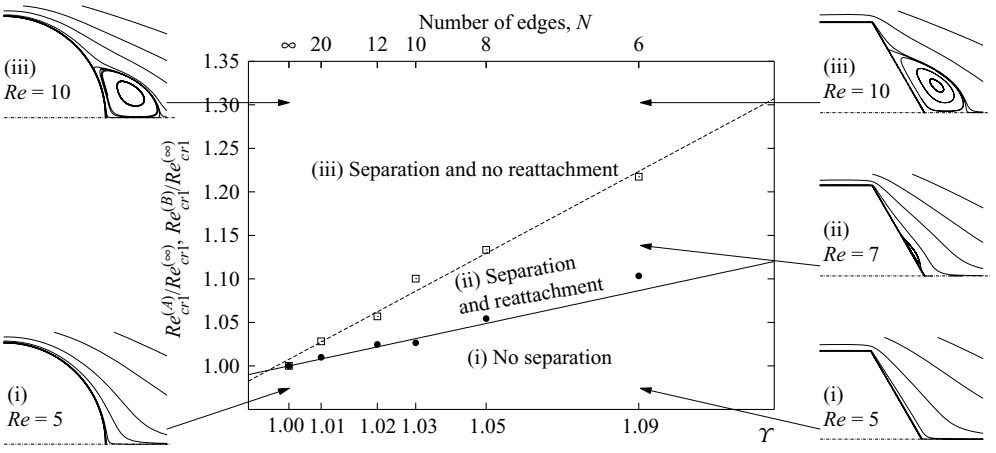


FIGURE 15. Re_{cr1} for N-sided polygons, —— $Re_{cr1}^{(A)}$, – – – $Re_{cr2}^{(B)}$, as well as the streamlines for flow past circles and hexagons.

3.2.3. *Flow patterns*

According to CFD results, the reattachment point is at the surface of polygons, when Re is slightly higher than the critical Reynolds number. However, for circles, the separated flow can only reattach at the symmetric axis behind the circles, and no reattachment is found on the surface. Figure 15 shows the different flow patterns for polygons and circles at different Reynolds numbers: $Re_{cr1}^{(A)}$ represents the critical Reynolds number when the separation firstly appears, and $Re_{cr1}^{(B)}$ represents the Reynolds number when the reattachment point coincides with the rear stagnation points. Beyond $Re_{cr1}^{(B)}$, no reattachment point can be found on the surface of polygons. For example, the flow past hexagons at $Re = 7$ is shown in figure 15, and we can find both the separation point and the reattachment point at the last edge. For circles, the two Reynolds numbers, $Re_{cr1}^{(A)}$ and $Re_{cr1}^{(B)}$, have the same value. As a result, the flow patterns with both separation and reattachment on the surface do not exist for flow past circles.

Next we shortly describe the streamline topologies before and after bifurcation. Brøns *et al.* (2007) studied the transition of streamline topologies for circular cylinders, and this transition can be described by a real parameter. When this parameter becomes negative from a positive number, the symmetric double-separation regions formed. They summarized the bifurcation as in figure 16(*a*), where the bifurcation point is at the rear stagnation point B. Before bifurcation, there is no critical point ahead of B, the bifurcation point, which is also a degenerated critical point. After bifurcation, there is only one saddle point on the wall, representing the separation, ahead of B.

For polygons, the bifurcation point is at A, ahead of B; we summarize this in figure 16(*b*). The bifurcation point A is not a critical point neither before nor after bifurcation. Before bifurcation, there is no critical point ahead of B, the rear stagnation point. However, slightly after bifurcation, there are two saddle points on the wall, ahead of B, representing the separation and reattachment, respectively.

We have shown that the Reynolds number for polygons in mapped domain is replaced by an equivalent one, $Re_{eq} = Re/\Upsilon$, and have conjectured the relationship for the critical Reynolds number (see (3.17)). However, the equivalent Reynolds number does not yield any difference, such as bifurcation point and streamline topology, in

https://doi.org/10.1017/S0022112009006168 Published online by Cambridge University Press

	Circles	Polygons
Critical Reynolds number	$Re_{cr1}^{(\infty)} \approx 6$	$Re_{cr1}^{(N)} \approx \Upsilon Re_{cr1}^{(\infty)}$
Bifurcation point	Rear stagnation point	Some point in the last edge, ahead of the rear stagnation point
Streamline topologies near surface	One saddle point ($Re > Re_{cr1}^{(\infty)}$)	Two saddle points ($Re_{cr1}^{(A)} < Re < Re_{cr1}^{(B)}$) One saddle point ($Re > Re_{cr1}^{(B)}$)

TABLE 1. Differences on appearance of separation between polygons and circles.

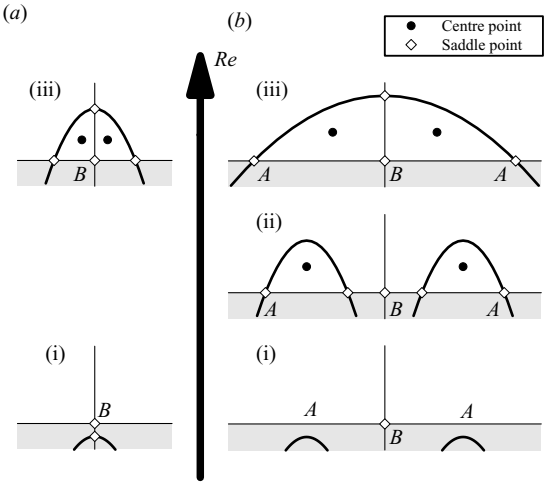


FIGURE 16. Bifurcation modes and streamline topologies near bifurcation points for (*a*) circles and (*b*) polygons, where the horizontal line represent the wall; the vertical line represents the symmetric plane; B is the rear stagnation point; A is a point ahead of B; and (i), (ii), and (iii) represent the regions in figure 15.

flow patterns between polygons and circles. We thus conjecture that this difference is caused by the non-null right-hand side of (3.11).

We summarize the differences between polygons and circles, on the appearance of separation, in table 1.

3.3. *Unsteady flows past polygons*

In this subsection we study the unsteady flow past polygons, addressing the relationships of flow features between polygons and circles, including Strouhal numbers, second critical Reynolds numbers and eigenvalues of the evolution of perturbations.

3.3.1. *Strouhal numbers*

Due to the appearance of the time-scaling factor in (3.14), we conjecture that the global Strouhal number for flow past polygons with a Reynolds number, Re, is approximately Υ times of that for the circular situation with a Reynolds number, Re_{eq}. The Strouhal number for flow past circular cylinders has been widely studied; e.g. Fey *et al.* (1998) proposed a linear relationship between St_∞ and $Re^{-1/2}$ based on

https://doi.org/10.1017/S0022112009006168 Published online by Cambridge University Press

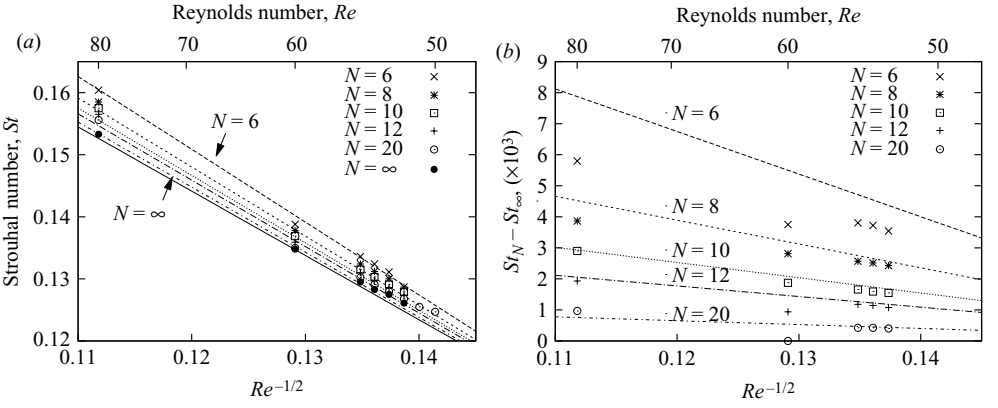


FIGURE 17. Strouhal numbers for flow past polygons and circular cylinders: (*a*) St_N and St_∞ versus $Re^{-1/2}$; (*b*) $St_N - St_\infty$ versus $Re^{-1/2}$.

experiments:

$$St_\infty = 0.2684 - 1.0356/\sqrt{Re}, \qquad (47 < Re < 180). \tag{3.20}$$

According to the above reasoning, we can replace Re in (3.20) with Re/Υ and multiply the result by Υ to obtain the Strouhal number for N-sided polygons. The expression thus obtained is

$$St_N \approx \Upsilon\left(0.2684 - 1.0356\sqrt{\frac{\Upsilon}{Re}}\right), \qquad (47 < Re/\Upsilon < 180), \tag{3.21}$$

where Υ is given by (B 7). Figure 17 displays the relationship between the Strouhal number and the Reynolds number. We also show the difference of Strouhal number between polygons and circular cylinders, $St_N - St_\infty$, varying with $Re^{-1/2}$. The lines in figure 17 are calculated by (3.21) and (3.20), while the points in the figure are measured from the CFD results, using a fast Fourier transform (FFT). We find from both the estimated results and the CFD results that the Strouhal numbers for polygons are monotonically decreasing functions of N. In figure 17, we find good coincidence between the estimated and CFD results for polygons with larger number of edge, e.g. $N = 10, 12, 20$, while for $N = 6, 8$, the estimated results are larger than the CFD results.

3.3.2. *Relations on eigenvalues between polygons and circles*

The transition from steady flow to unsteady flow belongs to a Hopf bifurcation with a complex characteristic parameters, $\sigma = \sigma_r + \mathrm{i}\sigma_i$. The real part σ_r represents the linear growth rate of perturbation, while the imaginary part σ_i represents the linear angular frequency. In order to analyse the relations of eigenvalues between polygons and circles, we recall the eigenvalue analysis for the circular situation (see Dušek *et al.* 1994).

The stream function is decomposed as $\psi = \psi_0 + \varphi$, where ψ_0 is the steady solution and φ is the perturbation. Both ψ and ψ_0 satisfy (3.14), so that

$$(\mathscr{S}\varphi)_t + \mathscr{L}[Re]\varphi + \mathscr{R}(\varphi, \varphi) = 0, \tag{3.22}$$

https://doi.org/10.1017/S0022112009006168 Published online by Cambridge University Press

where $\mathscr{S}$ denotes the Laplacian operator ∇^2 and $\mathscr{L}$ and $\mathscr{R}$ denote linear and quadratic operators, respectively. These operators are expressed as

$$\mathscr{S} = \nabla^2, \tag{3.23a}$$

$$\mathscr{L}[Re]\varphi = -\mathscr{J}(\psi_0, \nabla^2\varphi) - \mathscr{J}(\varphi, \nabla^2\psi_0) - \frac{2}{Re}(\nabla^4\varphi), \tag{3.23b}$$

$$\mathscr{R}(\varphi, \varphi) = -\mathscr{J}(\varphi, \nabla^2\varphi). \tag{3.23c}$$

The instability of the infinitely small perturbation φ depends linearly on the eigenfunction of the problem:

$$\left\{\mathscr{L}[Re] + \left(\sigma_r^{(j)} \pm \mathrm{i}\sigma_i^{(j)}\right)\mathscr{S}\right\}\phi_{\pm}^{(j)} = 0 \quad (j = 1, 2, \ldots), \tag{3.24}$$

where $\phi_{\pm}^{(j)}$ denotes the eigenfunction corresponding to the jth complex eigenvalue, $\sigma_r^{(j)} \pm \mathrm{i}\sigma_i^{(j)}$. If $\sigma_r^{(j)}$ is positive, the perturbation with an angular frequency $\sigma_i^{(j)}$ will amplify itself, and the steady flow will transform to the unsteady flow. Denote $\sigma = \sigma_r + \mathrm{i}\sigma_i$ as the eigenvalue with the largest real part. This can be regarded as the characteristic parameter of the Hopf bifurcation.

According to Schumm, Berger & Monkewitz (1994), the eigenvalue $\sigma = \sigma_r + \mathrm{i}\sigma_i$ has a linear relationship with the 'distance from criticality', $Re - Re_{cr2}$, when the system slightly exceeds the bifurcation point. By definition, the critical Reynolds number $Re_{cr2}^{(\infty)}$ satisfies $\sigma_r(Re_{cr2}^{(\infty)}) = 0$; hence one can expand $\sigma_r(Re)$ and $\sigma_i(Re)$ at Re_{cr2} as

$$\sigma_r(Re) = k_r^{(\infty)}\left(Re - Re_{cr2}^{(\infty)}\right), \tag{3.25a}$$

$$\sigma_i(Re) = \sigma_{i,0}^{(\infty)} + k_i^{(\infty)}\left(Re - Re_{cr2}^{(\infty)}\right). \tag{3.25b}$$

Here $\sigma_{i,0}^{(\infty)} = \sigma_i(Re_{cr2}^{(\infty)})$, $k_r^{(\infty)}$ and $k_i^{(\infty)}$ are the first-order derivative of $\sigma_r(Re)$ and $\sigma_i(Re)$ at Re_{cr2}.

For polygons, we follow the same analysis and decompose the stream function in mapped domain as $\tilde{\psi} = \tilde{\psi}_0 + \tilde{\varphi}$. Both $\tilde{\psi}$ and $\tilde{\psi}_0$ satisfy (3.13). Subtracting them, we obtain the equation for the perturbation $\tilde{\varphi}$:

$$\frac{\Upsilon}{\gamma^2}(\mathscr{S}\tilde{\varphi})_t + \mathscr{L}[Re_{eq}]\tilde{\varphi} + \mathscr{R}(\tilde{\varphi}, \tilde{\varphi}) = \hat{\mathscr{L}}[Re_{eq}]\tilde{\varphi} + \hat{\mathscr{R}}(\tilde{\varphi}, \tilde{\varphi}), \tag{3.26}$$

where $\mathscr{S}$, $\mathscr{L}$ and $\mathscr{R}$ are the same as circles if we drop the superscript '$\sim$' and change Re_{eq} to Re. However, the additional linear and quadratic operators $\hat{\mathscr{L}}$ and $\hat{\mathscr{R}}$ on the right-hand side of (3.26), which comes from the additional source terms in (3.13), are expressed as

$$\hat{\mathscr{L}}[Re_{eq}]\tilde{\varphi} = \frac{2}{Re_{eq}}\left(\frac{\tilde{\nabla}^2\gamma^2}{\gamma^2}\right)(\tilde{\nabla}^2\tilde{\varphi}) + \frac{4}{Re_{eq}}\left(\frac{\tilde{\nabla}\gamma^2}{\gamma^2}\right)\cdot[\tilde{\nabla}(\tilde{\nabla}^2\tilde{\varphi})] + \frac{1}{\gamma^2}\tilde{\mathscr{J}}(\tilde{\psi}_0, \gamma^2)(\tilde{\nabla}^2\tilde{\varphi}) + \frac{1}{\gamma^2}\mathscr{J}(\tilde{\varphi}, \gamma^2)(\nabla^2\tilde{\psi}_0), \tag{3.27a}$$

$$\hat{\mathscr{R}}(\tilde{\varphi}, \tilde{\varphi}) = \frac{1}{\gamma^2}\mathscr{J}(\tilde{\varphi}, \gamma^2)(\nabla^2\tilde{\varphi}). \tag{3.27b}$$

The corresponding linear eigenvalue problems for polygons and circles are given by

$$\left\{\mathscr{L}[Re_{eq}] - \hat{\mathscr{L}}[Re_{eq}] + \frac{\Upsilon}{\gamma^2}\left(\tilde{\sigma}_r^{(j)} \pm \mathrm{i}\tilde{\sigma}_i^{(j)}\right)\mathscr{S}\right\}\tilde{\phi}_{\pm}^{(j)} = 0 \quad (j = 1, 2, \ldots), \tag{3.28a}$$

https://doi.org/10.1017/S0022112009006168 Published online by Cambridge University Press

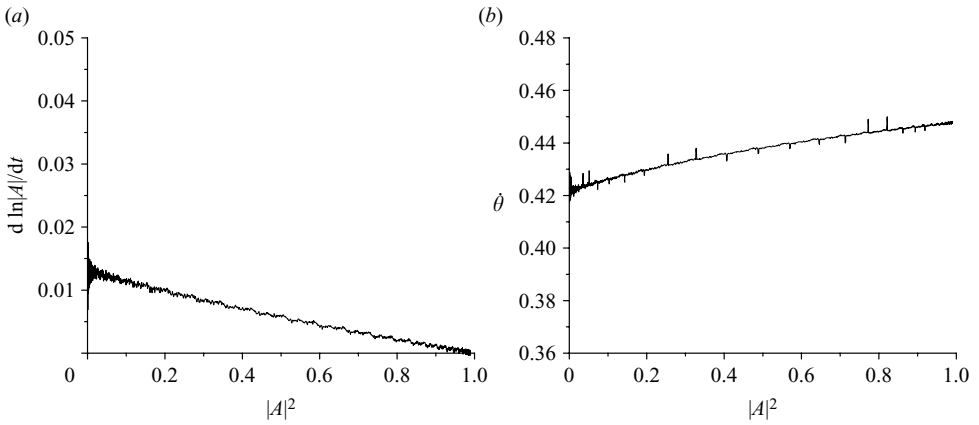


FIGURE 18. Evolution of perturbation for hexagons at $Re = 55$: (a) amplified rate versus $|A|^2$; (b) $\dot{\theta}$ versus $|A|^2$.

where $\tilde{\phi}_{\pm}^{(j)}$ denotes the eigenfunction corresponding to the jth complex eigenvalue $\tilde{\sigma}_r^{(j)} \pm \mathrm{i}\tilde{\sigma}_i^{(j)}$ for polygons. Suppose $\tilde{\sigma}_r + \mathrm{i}\tilde{\sigma}_i$ for polygons is the eigenvalue with the largest real part.

From (3.28a) it is clear that the eigenvalues for polygons differ from those for circles because of three factors: (i) time-scaling factor γ^2/Υ, (ii) equivalent Reynolds number Re_{eq} and (iii) additional linear operator $\hat{\mathscr{L}}[Re_{eq}]$ due to source term. As stated in the end of § 3.1, the influence due to source term is not considered in this paper.

Replacing Re in (3.24) with Re_{eq} and comparing the result with (3.28a) we obtain the following relationship of eigenvalues:

$$\tilde{\sigma}_r(Re) + \mathrm{i}\tilde{\sigma}_i(Re) = \Upsilon[\sigma_r(Re_{eq}) + \mathrm{i}\sigma_i(Re_{eq})]. \tag{3.29}$$

Substituting (3.25) into (3.29) and replacing Re_{eq} by Re/Υ, we obtain the real and imaginary parts of eigenvalues for polygons:

$$\tilde{\sigma}_r(Re) = k_r^{(\infty)}\left[Re - \Upsilon Re_{cr2}^{(\infty)}\right], \tag{3.30a}$$

$$\tilde{\sigma}_i(Re) = \Upsilon\sigma_{i,0}^{(\infty)} + k_i^{(\infty)}\left[Re - \Upsilon Re_{cr2}^{(\infty)}\right]. \tag{3.30b}$$

Equation (3.30) means that the eigenvalues depend linearly on Υ. This linear property will be checked by CFD below.

The eigenvalues can be obtained using the time evolution of the lift coefficients given by CFD (see Thompson & Gal 2004). This is done as follows: Suppose a complex perturbation is expressed as $A(t) = |A|(t)\mathrm{e}^{\mathrm{i}\theta(t)}$, where $|A|$ and θ are its amplitude and phase angle. The time evolution of the complex amplitude function $|A|$ and θ can be written as (see Thompson & Gal 2004).

$$\frac{\mathrm{d}\ln|A|}{\mathrm{d}t} = \tilde{\sigma}_r(1 - c_r|A|^2), \dot{\theta} = \tilde{\sigma}_i - \tilde{\sigma}_r c_i|A|^2, \tag{3.31}$$

where c_r and c_i are functions of $|A|^2$. Here we use the lift coefficient (obtained by CFD) as the global perturbation. Its complex value is obtained by a Hilbert transformation. Figure 18 shows the logarithmic derivative of the amplitude and the angular frequency on the square of the amplitude, and the intercepts are $\tilde{\sigma}_r$ and $\tilde{\sigma}_i$ respectively.

https://doi.org/10.1017/S0022112009006168 Published online by Cambridge University Press

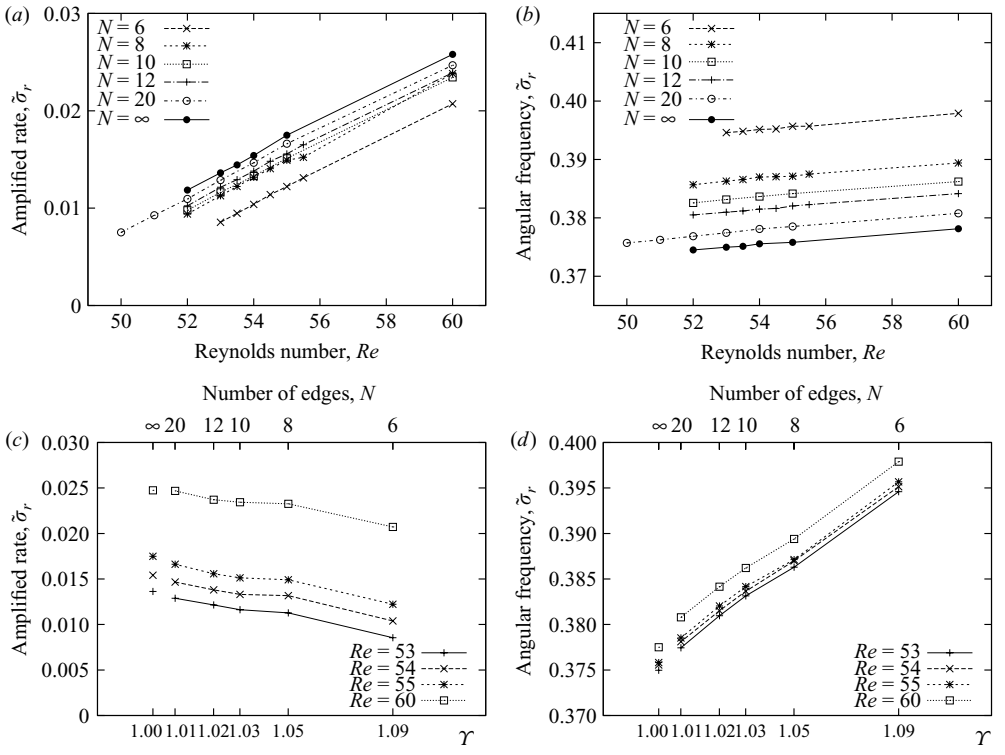


FIGURE 19. Eigenvalues for flow past polygons and circular cylinders: (*a*) $\tilde{\sigma}_r$ versus Re; (*b*) $\tilde{\sigma}_i$ versus Re; (*c*) $\tilde{\sigma}_r$ versus Υ; (*d*) $\tilde{\sigma}_i$ versus Υ.

Using this method, we can find the relationship between the eigenvalues $\tilde{\sigma}_r + \mathrm{i}\tilde{\sigma}_i$ and Re. Figure 19(*a*, *b*) displays the eigenvalues thus obtained, for both polygons and circles. The amplified rate $\tilde{\sigma}_r$ for polygons is slightly smaller than that for circles, while the angular frequency $\tilde{\sigma}_i$ is larger than that for circles. A linear relationship between eigenvalues and Υ is found (see figure 19*c*, *d*). This confirms the linear relation as in (3.30). Thus, the differences of eigenvalues between polygons and circular cylinders vanish linearly as Υ limits to unit (as N increases).

3.3.3. *Critical values: second critical Reynolds numbers and linear angular frequencies*

We use (3.30) to get the second critical Reynolds number for polygons. Setting $\tilde{\sigma}(Re_{eq2}^{(N)}) = 0$ in (3.30*a*), we obtain

$$Re_{cr2}^{(N)} = \Upsilon Re_{cr2}^{(\infty)} = \frac{N}{\pi} \sin\left(\frac{N-1}{N}\pi\right) \Gamma\left(\frac{N-1}{N}\right)^2 \Gamma\left(\frac{N+2}{N}\right) Re_{cr2}^{(\infty)}. \tag{3.32}$$

Equation (3.32) can also be obtained similarly as for the first critical Reynolds number through the use of equivalent Reynolds number. Setting $Re = Re_{cr2}^{(N)}$ in (3.30*b*), we find

$$\sigma_{i,0}^{(N)} = \Upsilon \sigma_{i,0}^{(\infty)} = \frac{N}{\pi} \sin\left(\frac{N-1}{N}\pi\right) \Gamma\left(\frac{N-1}{N}\right)^2 \Gamma\left(\frac{N+2}{N}\right) \sigma_{i,0}^{(\infty)}. \tag{3.33}$$

In order to check the above results, we use CFD to obtain $Re_{cr2}^{(N)}$ and $\sigma_{i,0}^{(N)}$ (see Sohankar 2007). Once $\tilde{\sigma}_r + \mathrm{i}\tilde{\sigma}_i$ is obtained by CFD combined with (3.31) for various

https://doi.org/10.1017/S0022112009006168 Published online by Cambridge University Press

Shape	N	Υ	$Re_{cr2}^{(N)}$	$\sigma_{i,0}^{(N)}$
Hexagon	6	1.0865	47.9890	0.3922
Octagon	8	1.0448	46.6910	0.3835
Decagon	10	1.0314	46.1826	0.3801
Dodecagon	12	1.0219	45.8715	0.3777
Icosagon	20	1.0080	45.5801	0.3736
Circle	∞	1.0000	45.1464	0.3714

TABLE 2. Comparison amongst N-sided polygons and circular cylinder about critical Reynolds numbers and linear angular frequencies.

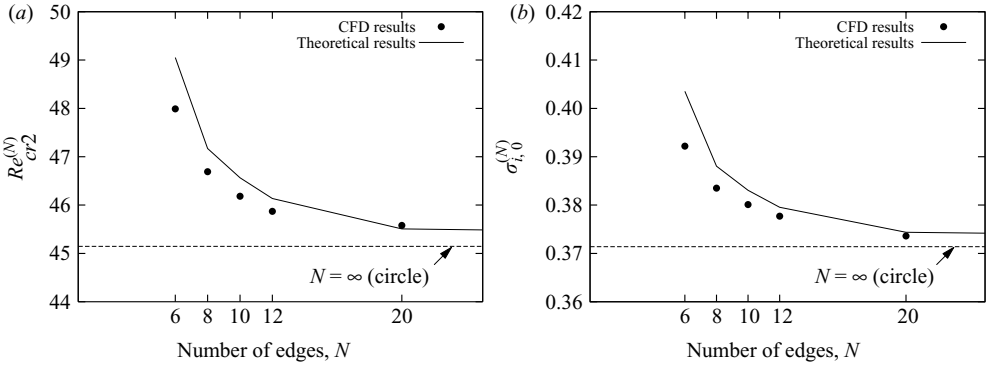


FIGURE 20. The critical values, (*a*) $Re_{cr2}^{(N)}$, (*b*) $\sigma_{i,0}^{(N)}$, for various N-sided polygons.

Reynolds numbers, we build a fitted function between $\tilde{\sigma}_r + \mathrm{i}\tilde{\sigma}_i$ and Re. Then we calculate the critical Reynolds number $Re_{cr2}^{(N)}$ by setting $\tilde{\sigma}_r(Re_{cr2}^{(N)}) = 0$, as well as $\sigma_{i,0}^{(N)}$, the value of $\tilde{\sigma}_i(Re)$ at $Re_{cr2}^{(N)}$. The fitted values for $Re_{cr2}^{(N)}$ and $\sigma_{i,0}^{(N)}$ are given in table 2. We see that $Re_{cr2}^{(N)}$ and $\sigma_{i,0}^{(N)}$ for polygons are both monotonically decreasing functions of N.

Figure 20 shows $Re_{cr2}^{(N)}$ and $\sigma_{i,0}^{(N)}$ in table 2 for each N-sided polygon. From figure 20(*a*), we find that (3.32) slightly overestimated Re_{cr2} and $\sigma_{i,0}$ as compared to CFD. But the qualitative agreement is well. Hence the critical Reynolds number for polygon is a monotonically decreasing function of N.

4. Conclusions

In this paper, we have studied the two-dimensional inviscid flow and low-Reynolds-number viscous flow past regular polygons, which have arbitrary but even numbers of edges and have one apex pointing to the incoming free stream. We have compared the flow past polygons with that past circular cylinders.

For the pure potential flow past polygons, an explicit formula exists for the pressure coefficient, and this is given by (2.3). Compared to the case of circular cylinder which only exhibits smooth flow, singularity around each apex is observed. The intensity of the singularity weakens when N increases, which can be seen through the N-variation of the radius ρ of the low-pressure region and of the global pressure difference Δ_{C_p} along the surface, satisfying $\rho \sim \mathrm{e}^{-N}$ and $\Delta_{C_p} \sim 1/N$ (for N large enough) respectively.

https://doi.org/10.1017/S0022112009006168 Published online by Cambridge University Press

The relationship between vortex motion for polygons in mapped domain, and that of circular cylinders is given by (2.15). Comparing with the circular situation, a rotation by the additional velocities and a scaling by γ^2 are added to the polygonal situation.

There are some additional closed lines for a univalent stationary vortex pair for separated flow polygons. These lines start from one apex and end at a certain edge or another apex. The stabilities on these lines are concerned with ρ, the distance to the centre, independent of perturbation modes. The vortex pair is neutral stable when ρ is less than a critical distance, while it is unstable when ρ is larger than that.

For the viscous flow past polygons, we derived equation of the stream function in the mapped (circle) domain (see (3.13)). Through this equation, we see that, compared to circular cylinders, the time scale is multiplied by Υ; the Reynolds number is replaced by the equivalent Reynolds number, $Re_{eq} = Re/\Upsilon$; and three additional source terms appeared.

For the steady separated flow, we found the critical Reynolds number, based on the diameter of the circumscribed circular cylinder, is given by $Re_{cr1}^{(N)} \approx \Upsilon Re_{cr1}^{(\infty)}$. It is a monotonically decreasing function of N. The CFD result follows roughly well, though not exactly, with $Re_{cr1}^{(N)} \approx \Upsilon Re_{cr1}^{(\infty)}$. For example, $Re_{cr1} \approx 6.64$ for a hexagon, corresponding to $Re_{cr1} \approx 6.02$ for circular cylinder. The bifurcation point at which separation first appears for polygons locates on the last edge, in contrast with the circular-cylinder case, for which the bifurcation point locates at the rear stagnation point. When Re is slightly larger than the first critical Reynolds number, reattachment is found on the surface of polygons, while for circular cylinders, there is no reattachment on the surface. The bifurcation point is a function of N (see figure 13).

For the unsteady flow, we found the critical Reynolds number and Strouhal number, based on the diameter of the circumscribed circular cylinder, are given by $Re_{cr2}^{(N)} \approx \Upsilon Re_{cr2}^{(\infty)}$ and $St_N \approx \Upsilon \left(0.2684 - 1.0356\sqrt{\Upsilon/Re}\right)$, respectively. They are both monotonically increasing functions of N; for example, $Re_{cr2} \approx 48$ for a hexagon, and $Re_{cr2} \approx 44.42$ for circular cylinder. The Strouhal numbers at critical Reynolds number for a hexagon and circular cylinder are 0.1226 and 0.1142, respectively.

Now we outline some subjects which need further study.

We know that the flow for higher Reynolds numbers is three-dimensional (see Coutanceau & Daefaye 1991; Williamson 1996). For the circular case, two modes exist: mode A appears at $Re_A \approx 188$–190 with a spanwise wavelength about $3D$–$4D$, and mode B appears at $Re_B \approx 230$–260 with a spanwise wavelength about D, where D stands for the diameter (see Zhang *et al.* 1995; Barkley & Henderson 1996; Williamson 1996). Square cylinder also has two transition modes, A and B (see Sohankar, Norberg & Davidson 1999; Luo, Chew & Ng 2003). For the square case, based on the Floquet instability analysis by Robichaux, Balachandar & Vanka (1999), $Re_A = 162$ and $Re_B = 190$, with the wavelength $5.22D_s$ and $1.2D_s$ separately, where D_s stands for the side length of square cylinder. According to the numerical results by Saha, Biswas & Muralidha (2003), $Re_A = 150$–175 with the wavelength $3D_s$, and $Re_B > 240$ with the wavelength $1.2D_s$–$1.4D_s$. As Re further increases, the flow past cylinders will experience shear layer transition and boundary layer transition and finally form turbulence flow. For polygons with more edges, the condition for transition and the different modes should be further studied.

In this paper, we didn't consider polygons with one edge facing the free stream and polygons with odd number of edges. According to known results for triangle (odd number) and square (one edge facing the free stream), the corresponding flow

https://doi.org/10.1017/S0022112009006168 Published online by Cambridge University Press

may be quite different. For example, for square cylinder, $N=4$ and $\Upsilon=1.1981$, the use of (3.19) would give $Re_{cr1}^{(4)}\approx 7.2$, while Franke (1991) obtained $Re_{cr1}^{(4)}<1$. The difference comes from the square cylinder in Franke (1991) having an edge facing the free stream, in contrast with the present paper for which an apex points to the free stream. For the polygon with odd number of edges, e.g. triangular cylinder, $N=3$ and $\Upsilon=1.2866$, the use of (3.19) would give $Re_{cr1}^{(3)}\approx 7.7$ if we had suppose it to be valid for odd edge numbers, while in reality the recirculation length at $Re_{cr1}^{(3)}$ is 0.58 times of the base length, according to the fit formula by De & Dalal (2006), and this means the flow has already separated. Hence, further studies on the effect of orientation of incoming flow and odd number of edges are needed for polygons with more edges. The drag coefficient and recirculation length for polygons with arbitrary N also need be studied in the future.

We would like to thank the referees for their useful comments concerning the use of reference length, conformal mapping and the like. Equation (3.15) was provided by one of the reviewers. This work has been supported by the 211 and the 985 Program of Tsinghua University.

Appendix A. Schwarz–Christoffel mapping of the exterior of unit circle into the exterior of its inscribed regular polygon with even number of edges

The Schwarz–Christoffel transformation is a complicated integral expression for an arbitrary polygon. Sandy (1970) expanded this integral into a summation of series with under-determined coefficients using a binomial theorem. For the regular polygon with even number of edges inscribed on a unit circle, we show that the coefficients can be expressed explicitly with the edge number, N.

The Schwarz–Christoffel mapping of the unit circle onto the outside of a general N-sided polygon is

$$z=f(\zeta)=A+B\int_1^{\zeta}\prod_{k=1}^{N}\left(1-\frac{a_k}{\zeta}\right)^{\beta_k}\mathrm{d}\zeta,\quad (z\in\mathscr{D}_N,\quad \zeta\in\tilde{\mathscr{D}}), \tag{A 1}$$

where A is a translation constant; B is a complex constant whose magnitude allows for a magnification and its argument for a rotation; a_k is a point on $|\zeta|=1$ corresponding to the kth apex of the polygon; and $\beta_k\pi$ is the exterior angle of kth apex of the polygon, $(k=1,2,\ldots,N)$.

By central symmetry for regular polygons, the coefficient a_k and β_k, $k=1,2,\ldots,N$, satisfy $\prod a_k=1$ and $\beta_k=2/N\equiv\beta$. Substituting these into (A 1), the integrand function can be simplified and expanded by the binomial theorem into a series, which gives

$$\prod_{k=1}^{N}\left(1-\frac{a_k}{\zeta}\right)^{\beta_k}=\left(1-\frac{1}{\zeta^N}\right)^{2/N}\equiv 1+\frac{\varepsilon_1}{\zeta^N}+\frac{\varepsilon_2}{\zeta^{2N}}+\frac{\varepsilon_3}{\zeta^{3N}}+\cdots, \tag{A 2}$$

where $\epsilon_k=\binom{2/N}{k}$ is the binomial coefficient. Substituting (A 2) into (A 1) and integrating the result term by term, we obtain

$$z=f(\zeta)=A+B\left(\zeta+\frac{\mathrm{e}_1}{\zeta^{N-1}}+\frac{\mathrm{e}_2}{\zeta^{2N-1}}+\frac{\mathrm{e}_3}{\zeta^{3N-1}}+\cdots\right), \tag{A 3}$$

where

$$\mathrm{e}_k=\frac{(-1)^{k-1}}{kN-1}\binom{2/N}{k}=\frac{(-1)^{k-1}}{kN-1}\frac{\Gamma(2/N+1)}{\Gamma(k+1)\Gamma(2/N-k+1)}\qquad (k=1,2,\ldots). \tag{A 4}$$

https://doi.org/10.1017/S0022112009006168 Published online by Cambridge University Press

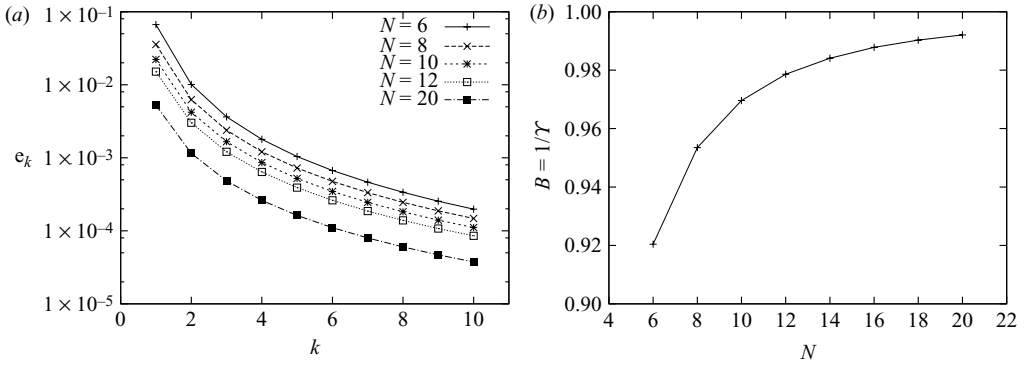


FIGURE 21. Coefficients in Schwarz–Christoffel mapping formula for various inscribed polygons: (*a*) e_k; (*b*) B.

For the regular polygons considered in this paper, two opposite apices lie in the horizontal symmetric axis, which means $\pm1 = f(\pm1)$. Substituting the two conditions into (A 3), the coefficient A and B can be solved as $A = 0$ and

$$B = \left[\frac{N}{\pi}\sin\left(\frac{N-1}{N}\pi\right)\Gamma\left(\frac{N-1}{N}\right)^2\Gamma\left(\frac{N+2}{N}\right)\right]^{-1}. \tag{A 5}$$

Figure 21 shows e_k and B varying with N and k. It can be seen that B approaches one with increasing N, which represents the geometrical approximation from polygons to circles as the increasing of edge number.

In summary the Schwarz–Christoffel mapping of the exterior of the unit circle into the exterior of its N-sided inscribed regular polygon is expressed as

$$z = f(\zeta) = B\left(\zeta + \frac{e_1}{\zeta^{N-1}} + \frac{e_2}{\zeta^{2N-1}} + \frac{e_3}{\zeta^{3N-1}} + \cdots\right), \tag{A 6}$$

where B is calculated by (A 5) and e_k is calculated by (A 4).

Appendix B. Deformation factor

In this appendix, we derive the expression for the deformation factor γ^2 and for some of its combinations.

When the unit circle in mapped domain $\zeta = \xi + \mathrm{i}\eta \in \tilde{\mathscr{D}}$ is mapped into its N-sided inscribed regular polygons in physical domain $z = x + \mathrm{i}y \in \mathscr{D}_N$ by Schwarz–Christoffel mapping $z = f(\zeta)$, this mapping deforms the space under a certain rule. This deformation can be described as a gradient matrix $\boldsymbol{G}$

$$\boldsymbol{G} = \frac{\partial(x,y)}{\partial(\xi,\eta)} = \begin{pmatrix} x_\xi & x_\eta \\ y_\xi & y_\eta \end{pmatrix} = \begin{pmatrix} \mathrm{Re}(f') & -\mathrm{Im}(f') \\ \mathrm{Im}(f') & \mathrm{Re}(f') \end{pmatrix}, \tag{B 1}$$

where the last equality is derived by Cauchy–Riemann condition. Hence $x_\xi = y_\eta = \mathrm{Re}(f')$ and $y_\xi = -x_\eta = \mathrm{Im}(f')$. Decompose the gradient matrix (B 1) into a symmetric matrix $\boldsymbol{S}$ and an antisymmetric matrix $\boldsymbol{\Omega}$, which are expressed as $\boldsymbol{S} = \mathrm{Re}(f')\mathbb{I}$ and $\boldsymbol{\Omega} = \mathrm{Im}(f')\mathbb{J}$, where $\mathbb{I}$ is a 2×2 unit matrix and $\mathbb{J}$ is a 2×2 unit symplectic matrix. The symmetric matrix $\boldsymbol{S}$ represents an isotropic stretch without shear, while the

https://doi.org/10.1017/S0022112009006168 Published online by Cambridge University Press

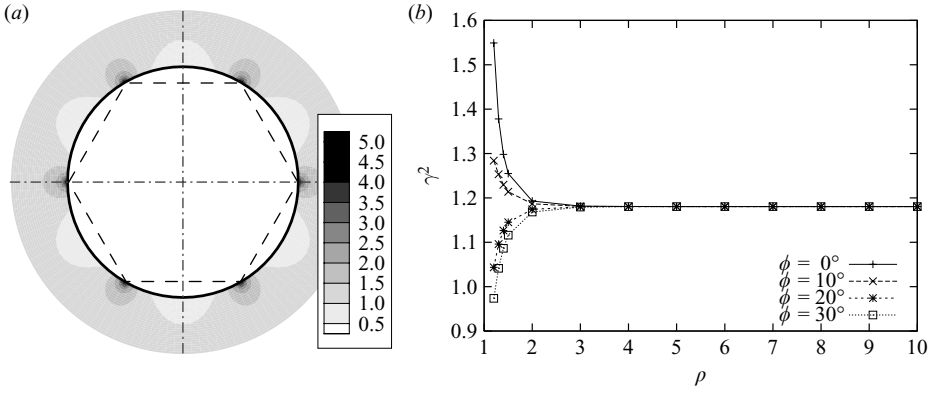


FIGURE 22. (*a*) Contour and (*b*) radial distribution of deformation factor, γ^2, in mapped domain.

antisymmetric matrix $\boldsymbol{\Omega}$ represents a rotation. The deformation factor γ^2, which is defined by $\gamma^2 = 1/|f'|$, is related to $\boldsymbol{S}$ and $\boldsymbol{\Omega}$ by

$$\boldsymbol{S}^2 - \boldsymbol{\Omega}^2 = |f'^2|\mathbb{I} = \frac{1}{\gamma^2}\mathbb{I} = \begin{pmatrix} \frac{1}{\gamma^2} & 0 \\ 0 & \frac{1}{\gamma^2} \end{pmatrix}. \tag{B 2}$$

Now we discuss the distribution of deformation factor γ^2 in mapped domain. According to (A 1) and (A 2), the derivative of Schwarz–Christoffel mapping $z = f(\zeta)$ can be expressed as

$$f'(\zeta) = B\left(1 - \frac{1}{\zeta^N}\right)^{2/N}. \tag{B 3}$$

Substituting (B 3) and (A 5) into $\gamma^2 = 1/|f'|$ and using $\zeta = \rho e^{i\phi}$, we obtain the explicit equation for γ^2:

$$\gamma^2 = \frac{1}{B^2}\left(1 - \frac{2\cos N\phi}{\rho^N} + \frac{1}{\rho^{2N}}\right)^{-2/N}. \tag{B 4}$$

Figure 22 shows the distribution of γ^2 in mapped domain for hexagons. As can be seen from figure 22(*a*), a maximum value is reached at $\phi = 0°, 60°$, representing the apices of hexagons, while a minimum value is reached at $\phi = 30°$, representing the midpoint of the edges. When ρ increases, γ^2 quickly approaches γ_∞^2, its value at infinity. Expanding (B 4) by Taylor expansion for $\rho \gg 1$, we obtain

$$\gamma^2 = \frac{1}{B^2} + \frac{4\cos N\phi}{NB^2\rho^N} + \ldots \approx \frac{1}{B^2}(\rho \gg 1), \tag{B 5}$$

where the residual vanishes with the $-N$ power as the increase of ρ. We denote

$$\Upsilon = \lim_{\rho\to\infty} \gamma. \tag{B 6}$$

Using (B 5) and (A 5), we find

$$\Upsilon = \frac{1}{B} = \frac{N}{\pi}\sin\left(\frac{N-1}{N}\pi\right)\Gamma\left(\frac{N-1}{N}\right)^2\Gamma\left(\frac{N+2}{N}\right). \tag{B 7}$$

For all polygons, we have $B < 1$ and $\Upsilon^2 > 1$.

https://doi.org/10.1017/S0022112009006168 Published online by Cambridge University Press

The expressions

$$\frac{\tilde{\nabla}^2\gamma^2}{\gamma^2} = \frac{16}{\rho^2(\rho^{2N} - 2\rho^N \cos N\phi + 1)} \tag{B 8}$$

and

$$\frac{(\gamma^2)_\rho}{\gamma^2} = -\frac{4}{\rho}\left(\frac{\rho^N \cos N\phi - 1}{\rho^{2N} - 2\rho^N \cos N\phi + 1}\right), \tag{B 9a}$$

$$\frac{1}{\rho}\frac{(\gamma^2)_\phi}{\gamma^2} = -\frac{4}{\rho}\left(\frac{\rho^N \sin N\phi}{\rho^{2N} - 2\rho^N \cos N\phi + 1}\right) \tag{B 9b}$$

have been used in § 3.1. They can be easily derived by using (B 4).

The relationship between f''/f' and gradients of γ^2,

$$\left(\frac{f''}{f'}\right)_p = \frac{1}{2}\left[-\frac{(\gamma^2)_\xi}{\gamma^2} + \mathrm{i}\frac{(\gamma^2)_\eta}{\gamma^2}\right]_p, \tag{B 10}$$

has been used in § 2.2.1 and is derived below.

Let $f'(\zeta) = a(\xi, \eta) + \mathrm{i}b(\xi, \eta)$, where a and b are the real and imaginary parts of f', respectively. Through Cauchy–Riemann relation, we write $f'' = a_\xi + \mathrm{i}b_\xi = b_\eta - \mathrm{i}a_\eta$. So we get

$$\frac{f''}{f'} = \frac{aa_\xi + bb_\xi}{a^2 + b^2} - \mathrm{i}\frac{aa_\eta + bb_\eta}{a^2 + b^2}. \tag{B 11}$$

Substituting $f' = a + \mathrm{i}b$ into $\gamma^2 = 1/|f'|$, we have

$$\gamma^2 = \frac{1}{|f'|^2} = \frac{1}{a^2 + b^2}. \tag{B 12}$$

Using (B 12), we can easily obtain

$$\frac{(\gamma^2)_\xi}{\gamma^2} = -2\frac{aa_\xi + bb_\xi}{a^2 + b^2}, \quad \frac{(\gamma^2)_\eta}{\gamma^2} = -2\frac{aa_\eta + bb_\eta}{a^2 + b^2}. \tag{B 13}$$

Inserting (B 13) into (B 11), we obtain (B 10).

Appendix C. CFD used in this paper

The flow past polygons in this paper belongs to laminar flow with a low Reynolds number, which is relatively simple to simulate by CFD. Various CFD methods or softwares should yield the same results if the boundary conditions are properly defined and if the grid is refined enough. In this paper, we have used the commercial software FLUENT, because of its wide accessibility, to solve the two-dimensional, incompressible, laminar Navier–Stokes equations, where the temporal term is given by a second-order discretization method, and the spatial discretization is given by a third-order MUSCL scheme.

Below we use known results to demonstrate how computation is done in this paper and what its accuracy is. We have been very careful about the accuracy or grid convergence of the CFD computation. We use a $28D \times 16D$ computational domain (see figure 23*a*), where D is the diameter of circumscribed circles of polygons. The mesh used in this paper is displayed in figure 23 for hexagons. It contains 79 000 grids. The height of the first cell at polygon surface is $0.001D$, with a stretching factor of 1.05 in the normal direction of polygon-wall inside regions, and 360 points

https://doi.org/10.1017/S0022112009006168 Published online by Cambridge University Press

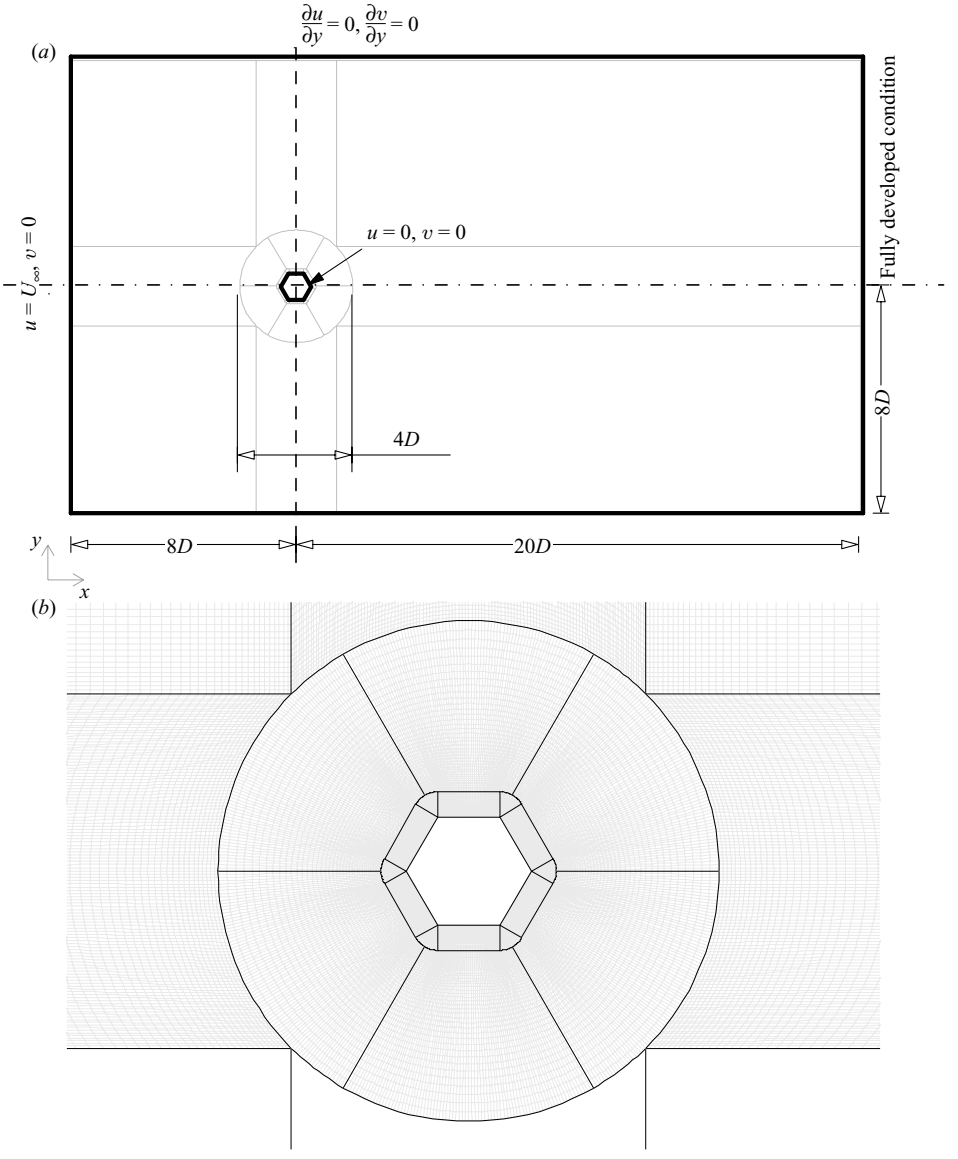


FIGURE 23. Sketch of the (*a*) computational domain, boundary conditions and (*b*) mesh grids for flow past polygons, e.g. hexagons

are located on the circumference of the polygons. Near the walls of polygons, the grids are meshed in a rectangle outside of each edge, for good orthogonality. Further refinement of the mesh grids and increase in the computational domain do not change the results.

The boundary conditions used in this paper are shown in figure 23(*a*) and are similar to those in Wu *et al.* (2004). A uniform flow condition is given at the inlet on the left-hand side of the computational domain, e.g. $u = U_\infty$ and $v = 0$. On the top and bottom sides, symmetric boundary conditions are given, e.g. $u_y = 0$ and $v_y = 0$.

https://doi.org/10.1017/S0022112009006168 Published online by Cambridge University Press

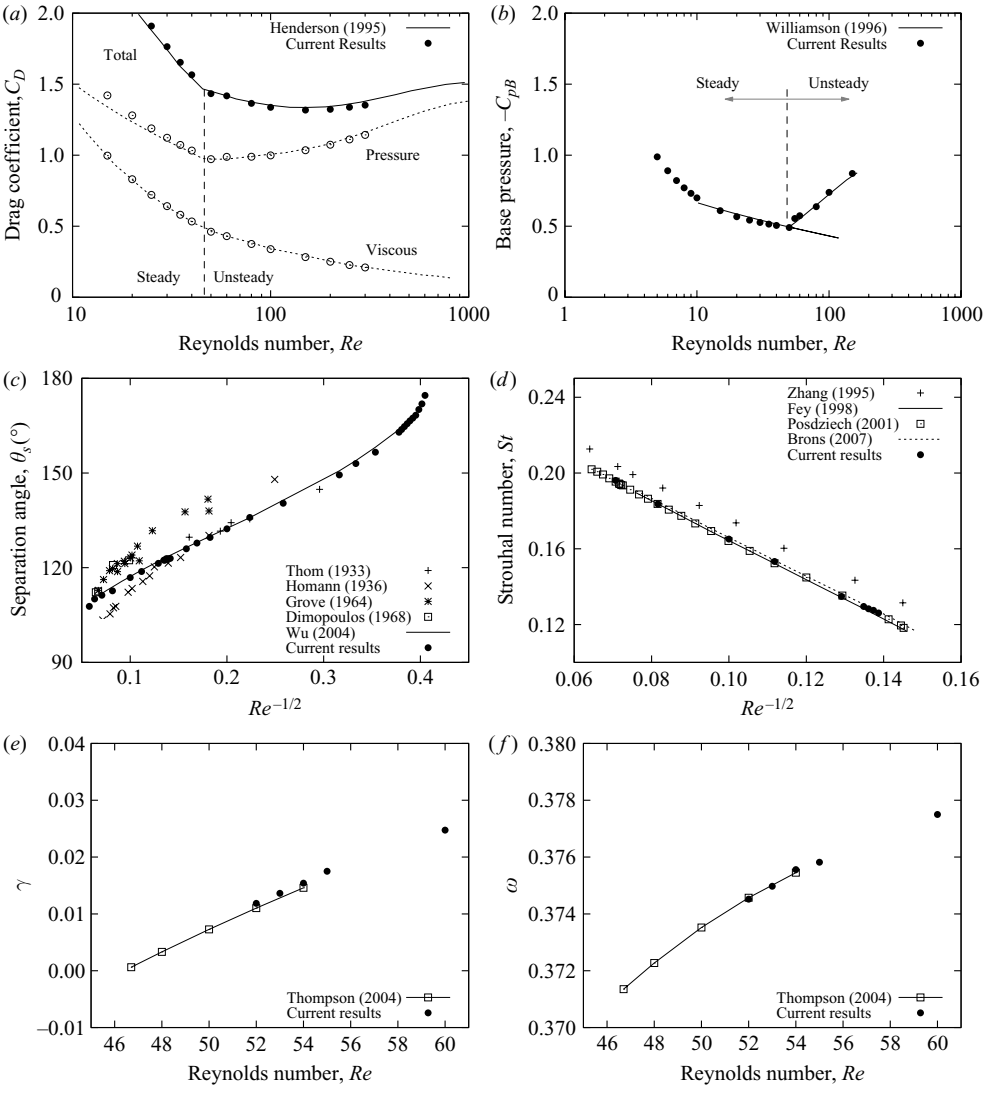


FIGURE 24. CFD results for flow past circles: (*a*) drag coefficient; (*b*) base pressure coefficient; (*c*) separation angle; (*d*) Strouhal number; (*e*) linear amplified rate; and (*f*) linear angular frequency.

On the right-hand side, a fully developed condition is used for the outflow of the velocity. On the polygons surface, the no-slip boundary condition $u = v = 0$ is given.

Now we use the method above to compute the flow past circular cylinder to check whether the result is accurate enough compared with the known results. Figure 24 shows the results for circles, including (*a*) drag coefficient, (*b*) base pressure coefficient, (*c*) separation angle, (*d*) Strouhal number, (*e*) linear amplified rate and (*f*) linear angular frequency. The results are very close to the known results.

In this paper, the same method has been used to compute the steady and unsteady flows past 6-, 8-, 10-, 12-, 20-sided regular polygons.

https://doi.org/10.1017/S0022112009006168 Published online by Cambridge University Press

REFERENCES

Abbassi, H., Turki, S. & Nasrallah, S. B. 2002 Channel flow past bluff-body: outlet boundary condition, vortex shedding and effects of buoyancy. *Comput. Mech.* **28**, 10–16.

Barkley, D. & Henderson, R. D. 1996 Three dimensional Floquet stability analysis of the wake of a circular cylinder. *J. Fluid Mech.* **322**, 215–241.

Batchelor, G. K. 1967 *An Introduction to Fluid Dynamics*. Cambridge University Press.

Breuer, M., Bernsdorf, J., Zeiser, T. & Durst, F. 2000 Accurate computations of the laminar flow past a square cylinder based on two different methods: lattice-Boltzmann and finite-volume. *Intl J. Heat Fluid Flow* **21**, 186–196.

Brøns, M., Jakobsen, B. & Niss, K. 2007 Streamline topology in the near wake of a circular cylinder at moderate Reynolds numbers. *J. Fluid Mech.* **584**, 23–43.

Cai, J., Liu, F. & Luo, S. J. 2003 Stability of symmetric vortices in two dimensions and over three-dimensional slender conical bodies. *J. Fluid Mech.* **480**, 65–94.

Clements, R. R. 1973 An inviscid model of two-dimensional vortex shedding. *J. Fluid Mech.* **57**, 321–336.

Coutanceau, M. & Daefaye, J. R. 1991 Circular cylinder wake configurations: a flow visualization survey. *Appl. Mech. Rev.* **44** (6), 255–305.

De, A. K. & Dalal, A. 2006 Numerical simulation of unconfined flow past a triangular cylinder. *Intl J. Numer. Mech. Fluids* **52**, 801–821.

Dennis, S. C. R. & Chang, G. Z. 1970 Numerical solutions for steady flow past a circular cylinder at Reynolds numbers up to 100. *J. Fluid Mech.* **42**, 379–399.

Dimopoulos, H. G. & Hanratty, T. J. 1968 Velocity gradients at the wall for flow around a cylinder for Reynolds numbers between 60 and 360. *J. Fluid Mech.* **33**, 303–319.

Dušek, J., Gal, P. L. & Fraunié, P. 1994 A numerical and theoretical study of the first Hopf bifurcation in a cylinder wake. *J. Fluid Mech.* **264**, 59–80.

Elcrat, A., Fornberg, B., Horn, M. & Miller, K 2000 Some steady vortex flows past a circular cylinder. *J. Fluid Mech.* **409**, 13–27.

Elcrat, A. R. & Trefethen, L. N. 1986 Classical free-streamline flow over a polygonal obstacle. *J. Comput. Appl. Math.* **14**, 251–265.

Fey, U., König, M. & Eckelmann, H. 1998 A new Strouhal–Reynolds-number relationship for the circular cylinder in the range $47 < re < 2 \times 10^5$. *Phys. Fluids* **10** (7), 1547–1549.

Föppl, L. 1913 Wirbelbewegung hinter einem kreiszylinder [Vortex motion behind a circular cylinder]. *Sitzb. d. k. baeyr, Akad. d. Wiss.* **1**, 1–17.

Franke, R. 1991 Numerische berechnung der instationären wirbelablösung hinter zylindrischen körpern. PhD thesis, University of Karlsruhe.

Grove, A. S., Shair, F. H., Petersen, E. E. & Acrivos, A. 1964 An experimental investigation of the steady separated flow past a circular cylinder. *J. Fluid Mech.* **19**, 60–81.

Henderson, R. D. 1995 Details of the drag curve near the onset of vortex shedding. *Phys. Fluids* **7** (9), 2102–2104.

Homann, F. 1936 Einfluss grsser zähigkeit bei strmung um zylinder. *Forsch. Ing. Wes.* **7**, 1–9.

Igarashi, T. 1997 Drag reduction of a square prism by the flow control using a small rod. *J. Wind Engng Indus. Aerodyn.* **69–71**, 141–153.

Igarashi, T. & Ito, S. 1993 Drag reduction of a square prism. Part 1. Flow control around a square prism using a small vortex shedder. *Trans. JSME* **59** (568), 3701–3707.

Jackson, C. P. 1987 A finite-element study of the onset of vortex shedding in flow past variously shaped bodies. *J. Fluid Mech.* **182**, 23–45.

Kiya, M., Saskai, K. & Arie, M. 1982 Discrete vortex simulation of a turbulent separation bubble. *J. Fluid Mech.* **120**, 219–244.

Klekar, K. M. & Patankar, S. V. 1992 Numerical prediction of vortex shedding behind square cylinders. *Intl J. Numer. Mech. Fluids* **14**, 327–341.

Lin, C. C. 1941*a* On the motion of vortices in two dimensions – I Existence of the Kirchhoff Routh function. *Proc. Natl Acad. Sci.* **27** (12), 570–575.

Lin, C. C. 1941*b* On the motion of vortices in two dimensions – II Some further investigations on the Kirchhoff Routh function. *Proc. Natl Acad. Sci.* **27**(12), 575–577.

Luo, S. C., Chew, Y. T. & Ng, Y. T. 2003 Characteristics of square wake transition flows. *Phys. Fluids* **15** (9), 2549–2559.

https://doi.org/10.1017/S0022112009006168 Published online by Cambridge University Press

Newton, P. K. 2000 *The N-Vortex Problem*. Springer.

Noack, B. R. & Eckelmann, H. 1994*a* A global stability analysis of the steady and periodic cylinder wake. *J. Fluid Mech.* **270**, 297–330.

Noack, B. R. & Eckelmann, H. 1994*b* A low-dimensional Galerkin method for the three-dimensional flow around a circular cylinder. *Phys. Fluids* **6**, 124–143.

Okajima, A. 1982 Strouhal numbers of rectangular cylinders. *J. Fluid Mech.* **123**, 379–398.

Posdziech, O. & Grundmann, R. 2001 Numerical simulation of the flow around an infinitely long circular cylinder in the transition regime. *Theoret. Comput. Fluid Dynamics* **15**, 121–141.

Protas, B. 2007 Center manifold analysis of a point-vortex model of vortex shedding with control. *Physica* D **228** (2), 179–187.

Robichaux, J., Balachandar, S. & Vanka, S. P. 1999 Three-dimensional Floquet instability of the wake of square cylinder. *Phys. Fluids* **11**, 560–578.

Routh, E. J. 1881 Some applications of conjugate functions. *Proc. Lond. Math. Soc.* **12**, 73–89.

Saffman, P. G. 1992 *Vortex Dynamics*. Cambridge University Press.

Saha, A. K., Biswas, G. & Muralidha, K. 2003 Three dimensional study of flow past a square cylinder at low Reynolds numbers. *Intl J. Heat Fluid Flow* **24**, 54–66.

Sakamoto, H., Tan, K., Takeuchi, N. & Haniu, H. 1997 Suppression of fluid forces acting on a square prism by passive control. *ASME J. Fluids Engng* **119**, 506–511.

Sandy, S. C. 1970 Evaluation of the Schwarz–Christoffel mapping function for special polygons. *SIAM J. Appl. Math.* **18** (4), 815–817.

Sarpkaya, T. 1975 An inviscid model of two dimensional vortex shedding for transient and asymptotically steady separated flow over an inclined plate. *J. Fluid Mech.* **68**, 109–128.

Schumm, M., Berger, E. & Monkewitz, P. A. 1994 Self-excited oscillations in the wake of two-dimensional bluff bodies and therir control. *J. Fluid Mech.* **271**, 17–53.

Sharma, A. & Eswaran, V. 2004 Heat and fluid flow across a square cylinder in the two-dimensional laminar flow regime. *Numer. Heat Transfer* A **45**, 247–269.

Shashikanth, B. N., Marsden, J. E., Burdick, J. W. & Kelly, S. D. 2002 The Hamiltonian structure of a two-dimensional rigid circular cylinder interacting dynamically with n point vortices. *Phys. Fluids* **14** (3), 1214–1227.

Skews, B. W. 1991 Autorotation of many-sided bodies in an airstream. *Nature* **352**, 512–513.

Skews, B. W. 1998 Autorotation of polygonal prisms with an upstream vane. *J. Wind Engng Indus. Aerodyn.* **73**, 145–158.

Sohankar, A. 2007 Hopf bifurcation, vortex shedding and near wake study of a heated cylinder in cross flow. *Iranian J. Sci. Technol.* **31** (B1), 31–47.

Sohankar, A., Norberg, C. & Davidson, L. 1999 Simulation of three dimensional flow around a square cylinder at moderate Reynolds numbers. *Phys. Fluids* **11**, 288–306.

Taneda, S. 1956 Experimental investigation of the wakes behind cylinders and plates at low Reynolds numbers. *J. Phys. Soc. Jpn* **11**, 347–384.

Tang, S. & Aubry, N. 1997 On the symmetry breaking instability leading to vortex shedding. *Phys. Fluids* **9** (9), 2550–2561.

Thom, A. 1933 The flow past circular cylinders at low speeds. *Proc. R. Soc. Lond.* A **141**, 651–669.

Thompson, M. C. & Gal, P. L. 2004 The stuart - landau model applied to wake transition revisited. *Eur. J. Mech.* B **23**, 219–228.

Tian, X. S. 1996 Wind tunnel test investigation and engineering application of 24 angular polygon section. *Acta Aerodyn. Sin.* **14** (4), 379–386.

Wesfreid, J. E., Goujon-Durand, S. & Zielinska, B. J. A. 1996 Global mode behavior of the streamwise velocity in wakes. *J. Phys. II France* **6**, 1343–1357.

Williamson, C. H. K. 1996 Vortex dynamics in the cylinder wake. *Annu. Rev. Fluid Mech.* **28**, 477–539.

Wu, M. H., Wen, C. Y., Yen, R. H., Weng, M. C. & Wang, A. B. 2004 Experimental and numerical study of the separation angle for flow around a circular cylinder at low Reynolds number. *J. Fluid Mech.* **515**, 233–260.

Zannetti, L. 2006 Vortex equilibrium in flow past bluff bodies. *J. Fluid Mech.* **562**, 151–171.

https://doi.org/10.1017/S0022112009006168 Published online by Cambridge University Press

Zebib, A. 1987 Stability of viscous flow past a circular cylinder. *J. Engng Maths* **21**, 155–165.

Zhang, H. Q., Fey, U., Noack, B. R., König, M. & Eckelmann, H. 1995 On the transition of the cylinder wake. *Phys. Fluids* **7** (4), 779–794.

Zhou, L., Cheng, M. & Hung, K. C. 2005 Suppression of fluid force on a square cylinder by flow control. *J. Fluids Struct*. **21**, 151–167.

Zielinska, B. J. A., Durand, S. G., Dušek, J. & Wesfreid, J. E. 1997 Strongly nonlinear effect in unstable wakes. *Phys. Rev. Lett*. **79**, 3893–3896.

Zielinska, B. J. A. & Wesfreid, J. E. 1995 On the spatial structure of global modes in wake flow. *Phys. Fluids* **7**, 1418–1424.

https://doi.org/10.1017/S0022112009006168 Published online by Cambridge University Press